

Development of HPC-based hydrothermal FE simulator using deal.II

Xiang Sun, Alp Cinar and Kenichi Soga
UC Berkeley

1. Introduction

The objective of this work is to develop a high performance computing (HPC) based hydrothermal finite element (FE) simulator that can simulate the subsurface and its hydrothermal status at tens of km-scale so that it becomes possible to investigate how the subsurface responds to the activities of underground utilization at regional-scale or city-scale. For any regional or city-scale geothermal installation there are multiple different possible designs that will in turn couple in different ways with natural and anthropogenic subsurface variability creating a complex multiparameter space that must be explored for design optimization. In addition to natural subsurface variability, the uneven spatial distribution of excess heat in the subsurface can be viewed analogously to that of the urban heat island effect observed in many mega cities. The combined effect of the urban heat island and underground heat island has enhanced the subsurface temperature in many areas by several degrees. With correct planning, this excess and unevenly distributed heat energy can be harnessed beneficially. However, if unchecked, it can result in high environmental and economic costs: (a) even a one-degree increase above assumed far-field temperatures can significantly affect the ventilation and cooling costs of underground spaces, (b) ground temperature influences the expected efficiency of geo-energy systems, (c) underground temperatures are coupled with groundwater flow, and both above and below-ground structures can impact the quality and quantity of groundwater flow, and (d) changes in ground temperature and groundwater flow can influence the health of underground structures and infrastructure. If the current spatio-temporal variability of ground temperatures is known and future changes can be predicted, it would enable sustainable and resilient planning of underground activities in communities for both the short and long-term. To investigate such large city-scale underground thermal behavior, an HPC-based hydrothermal subsurface simulator is needed.

In this study, a coupled hydrothermal simulator based on the open source finite element library deal.II was developed to estimate the heat response of subsurface system on a city/regional scale. The performance of the developed code was verified using a benchmark case study and compared to that of the commercial software COMSOL Multiphysics. To test the capacity of the HPC code, the use of a subsurface heat exchange system at Treasure Island was selected as a case study. The performance testing of this case study model with multiple processors show that multiple city-scale scenarios could be explored in a reasonable amount of time using this new code.

2. HPC simulator based on deal.II

To conduct a large-scale simulation, large computational resources are required. High-performance computing has thousands of cores and millions of elements, which can provide enough computing power to handle the proposed large-scale simulations. Many software products now have the feature of multi-threads and multi-nodes parallel computing compatibility such as COMSOL Multiphysics, Abaqus and

Ansys-Fluent, etc. However, these commercial software products have low flexibility in the further development of the model. deal.II is the successor to the Differential Equations Analysis Library, which is a C++ programming library and is used to solve partial differential equations (PDEs) numerically. The structure of deal.II is flexible and it has a powerful computational resource optimization with popular open-source libraries on parallel computing. A preferable computing scheme can be selected to obtain the most optimal solution for a specific problem of interest.

The programming scheme of the deal.II library for finite element simulation is shown in Fig. 1. It consists of nine modules including Triangulation, FiniteElement, Quadrature, Mapping, DoFHandler, FEValues, Linear Systems, Linear Solver and Output. The Triangulation module is used to collect the information of cells, low dimensional boundary, geometric shapes, topological properties and read or write a grid. It has an iterator to traverse all cells and ask for information about the cell. When programming needs to loop for cells, it can provide the iterator. The FiniteElement module describes the properties of a finite element space defined on the unit cell. It also provides values and gradients of individual shape functions at the point on the unit cell. The Quadrature module just operates in the unit cell. It describes the location and weights of quadrature points on the unit cell. The Mapping module is applied to map the shape functions, quadrature points, and quadrature weights from the unit cell to each cell of triangulation and describes how to map points from unit to real space and back, as well as provides the gradients of this derivative and Jacobian determinants. DoFHandler can allocate the space for vertices, lines and cells and also gives them global numbering. It also provides an iterator like the Triangulation module. The iterator is used to loop for cells and extract values corresponding to the degree of freedom on the cell. Similar to the Triangulation module, the FEValues module is to evaluate finite element shape functions and their gradients at the quadrature points defined by a quadrature formula when mapped to the real cell. The Linear Systems module assembles the system matrix and the right-side according to the shape function value and gradient on a single cell and the obtained global number of the degrees of freedom. It provides direct and iterative solvers to solve the linear system. It also involves many open-source linear solvers for parallel computing. The Output module arranges the data in a graphical output file format for plotting (Arndt et al. 2020).

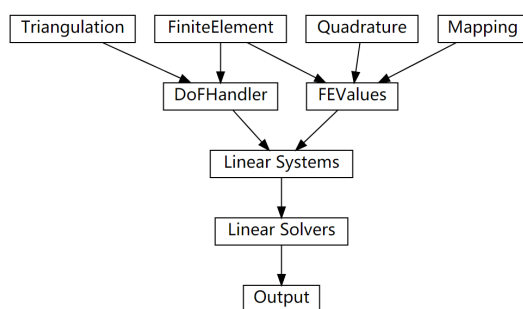


Fig. 1 The programming scheme of deal.II (Arndt et al. 2020)

3. Implementation of the discretized governing equations for subsurface heat and fluid transfer into deal.II

To obtain a linear system for the subsurface heat and fluid transfer, the discrete form of the governing equations needs to be established. The subsurface heat transfer is affected by the groundwater flow. When the groundwater flow velocity is high, the heat will transfer faster. In this study, it is assumed that

the problem is a one-way coupled hydrothermal process. The governing equations of the process are shown in Eq. 1 and 2.

$$\frac{1}{B_{poro}} \frac{dp}{dt} + \nabla \cdot (-k \cdot (\nabla p + \rho_w \mathbf{g})) = 0 \quad (1)$$

$$\frac{dT}{dt} + \nabla \cdot \left(-\frac{\lambda}{c_T} \nabla T \right) + \frac{c_w}{c_T} \mathbf{q} \cdot \nabla T = 0 \quad (2)$$

where

$$\lambda = (1 - \phi)\lambda_s + \phi\lambda_w$$

$$c_T = (1 - \phi)c_s + \phi c_w$$

$$k = \frac{K_i}{\mu_w} = \frac{K}{\rho_w g}$$

$$\mathbf{q} = -k(\nabla p + \rho_w \mathbf{g})$$

p is the water pressure, T is the temperature, λ_s is the thermal conductivity of solid, λ_w is the thermal conductivity of pore fluid, ϕ is the porosity, c_s is the heat capacity of solid, c_w is the heat capacity of pore fluid, B_{poro} is the porous compressibility, \mathbf{g} is the gravity acceleration, K_i is the permeability, μ_w is the viscosity of pore fluid, ρ_w is the density of pore fluid, K is the hydraulic conductivity and \mathbf{q} is the Darcy's flow velocity.

The finite element method with a backward Euler integral scheme is applied to obtain the discrete form of the governing equations given in Eqs. (1) and (2) as follows:

$$\begin{aligned} & hkB_{poro} \cdot (\nabla \mathbf{N}_p, \nabla \mathbf{N}_p)_\Omega \cdot \mathbf{P}^{n+1} + (\mathbf{N}_p, \mathbf{N}_p)_\Omega \cdot \mathbf{P}^{n+1} \\ &= -hB_{poro} (\mathbf{N}_p, \mathbf{q}^{n+1})_{\partial\Omega} + (\mathbf{N}_p, \mathbf{N}_p)_\Omega \cdot \mathbf{P}^n - \left(\nabla \mathbf{N}_p, hkB_{poro} \cdot (\rho_w \mathbf{g}) \right)_\Omega \end{aligned} \quad (3)$$

$$\begin{aligned} & (\mathbf{N}_T, \mathbf{N}_T)_\Omega \cdot \mathbf{T}^{n+1} + \frac{h\lambda}{c_T} (\nabla \mathbf{N}_T, \nabla \mathbf{N}_T)_\Omega \cdot \mathbf{T}^{n+1} + \left(\mathbf{N}_T, \frac{hc_w}{c_T} (-k(\nabla \mathbf{N}_p \cdot \mathbf{P}^{n+1} + \rho_w \mathbf{g})) \cdot \nabla \mathbf{N}_T \cdot \mathbf{T}^{n+1} \right) \\ &= -\frac{h}{c_T} (\mathbf{N}_T, -\lambda \nabla \mathbf{N}_T)_{\partial\Omega} \cdot \mathbf{T}^{n+1} + (\mathbf{N}_T, \mathbf{N}_T)_\Omega \cdot \mathbf{T}^n \end{aligned} \quad (4)$$

where \mathbf{N}_p and \mathbf{N}_T are the weight functions for discretized pressure and temperature, respectively, n is the n th time step, $(*,*)_\Omega$ is the inner product operator and h is the time step size.

Based on the discretized form, the programming scheme shown in **Fig. 2** is implemented. The grid can be directly imported into the deal.II programming. The DofHandler module is used to obtain the information on the degrees of freedom (DOFs). The initial conditions are applied using the linear interpolation method defined in the Vector class. Then, it is looped for cells and DOFs to form the cell-matrix and then the cell-matrix is assembled into the system matrix for the heat and flow equations. Because this problem is a sequential one-way coupling between the flow equation and the heat equation, the flow equation is solved first to obtain the solution of water pressure and pressure gradient. The pressure gradient is used to form the convection matrix in the heat equation to solve the temperature variation. The backward Euler method is used to carry out a stable time integral. When implementing a large time step, a large number of iterations for solving the linear system is needed to obtain a convergent solution. In some cases, the iteration number will be in excess of the preset maximum number leading to the termination of the computation. Therefore, when a large number of iterations is detected in the current time step, the time step size in the next time step is reduced by half to decrease the iteration number for

better convergence.

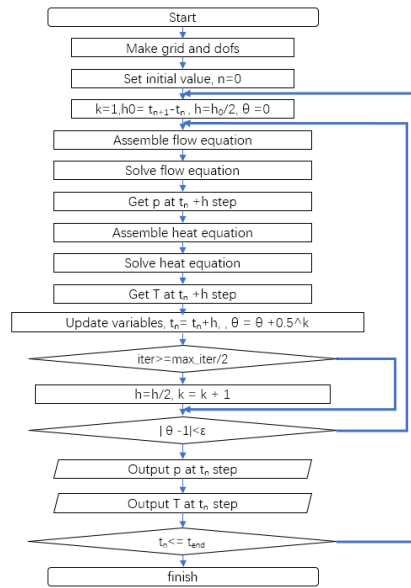


Fig. 2 Programming flow chat

Fig. 3 is an example showing how the initial conditions and boundary conditions are applied. An InitialValues function is defined and the initial condition can be applied by using the function of interpolation defined in the VectorTools class. **Fig. 4** shows the performance of the implementation. The Dirichlet boundary is implemented using the function of apply_boundary_values defined in the MatrixTools class. It can rearrange the system matrix and right-hand side vector to force the non-diagonal entry corresponding to the boundary nodes to be zero and diagonal entry equal to 1 in the system matrix. Then, the boundary values are placed to the corresponding locations in the right-hand side array. The Neumann boundary (Type 2) conditions are formed as the right-hand side in discrete form. **Fig. 5** shows the performance of these two types of boundary conditions, in which Boundary Type 1 is a Dirichlet boundary condition with a constant value. The other boundary conditions are set to Type 2, which is a Neumann boundary condition with a constant zero flux. The intersecting line between these boundaries yields the Type 2 boundary because, in this sample case, the Dirichlet boundary is applied before applying the Neumann boundary. The latter one overlaps the former one leading to the element along the intersecting line yielding to the Neumann boundary condition.

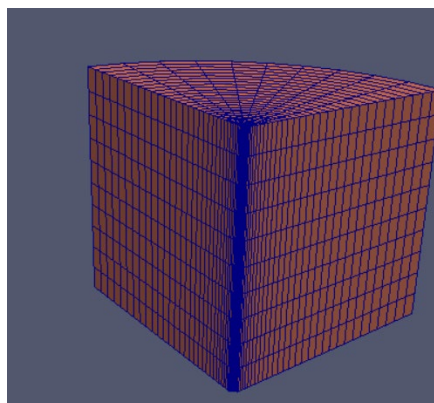


Fig. 3 Mesh of the example model

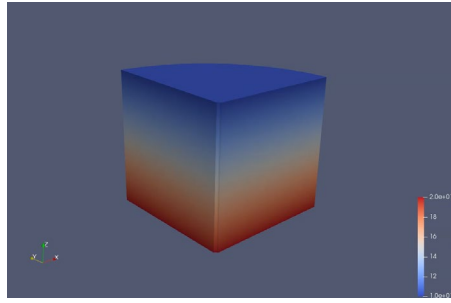


Fig. 4 The settings of initial values

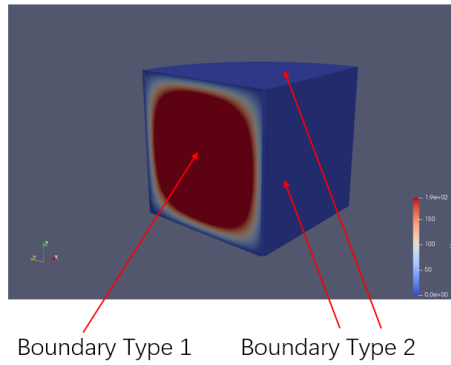


Fig. 5 The settings of boundary conditions

4. Verifications

To verify the performance of the developed code, a benchmark case study is set up and the results of the developed code are compared to those obtained using the commercial FE analysis software COMSOL Multiphysics. The benchmark case simulates the variation of underground temperature and pressure during hot water injection. This is a time-dependent process in which the duration of heating is set to one day. The geometry of the model, which is 1/4 of the whole system, is shown in **Fig. 6**. The radius of the model is 10 m and the height of the quarter column is set to be 10 m. A hole with a radius of 0.2 m is drilled at the center of the column. The mesh size is about 0.1 m around the hole and 0.5 m around outer boundary of the system. A water flow with a velocity of 0.001m/s and a temperature of 278.15K is injected from the borehole. The model parameters for the subsurface material are given in Table 1.

Table 1. Model parameters for the benchmark case

Parameter	Value	Unit	Comment
K	1×10^{-5}	m/s	Hydraulic conductivity
c_T	1.2×10^6	J/K/m ³	Heat capacity
λ	1.2	W/K/m	Heat conductivity
B_{poro}	1×10^5	Pa	Porous compressibility
T_0	273.15	K	Initial temperature
T_b	278.15	K	Wellbore temperature
P_0	0.1	MPa	Initial pressure
Q_b	0.001	m/s	Injection flux
C_w	1×10^6	J/K/m ³	Heat capacity of water

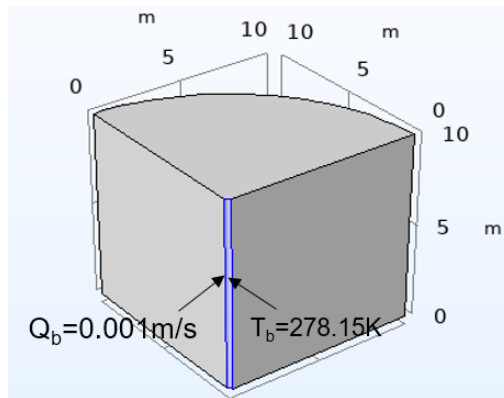


Fig. 6 Wellbore boundary condition

The simulation results of the water pressure given by COMSOL and deal.II are shown in Fig. 7(a) and (b), respectively. The distribution of the pressure is plotted in the radial direction on the first day. The two codes give the same pressure solution. The temperature profiles given by these two codes after one day of injection are compared in Fig. 9 and Fig. 10. The solution given by COMSOL has a small numerical instability due to the use of a low order element. Apart from the unstable part, the COMSOL solution generally matches well to the solution given by the developed deal.II code.

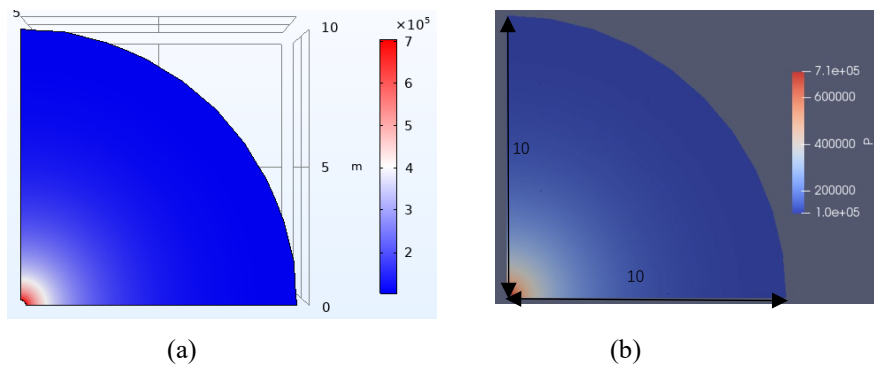


Fig. 7 Simulation results of pressure (Pa) given by (a) COMSOL (b) deal.II

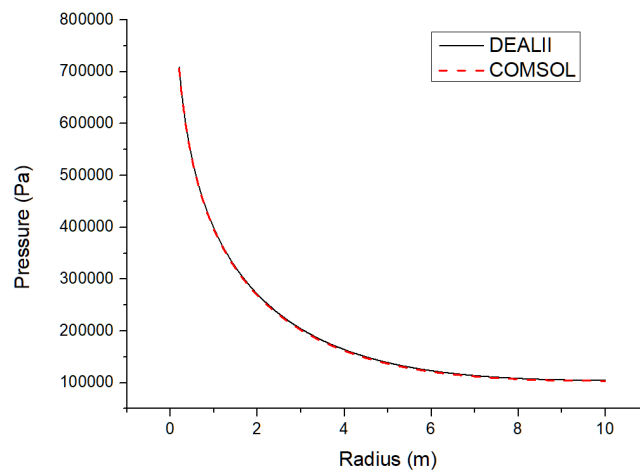


Fig. 8 Pressure distribution in the r direction

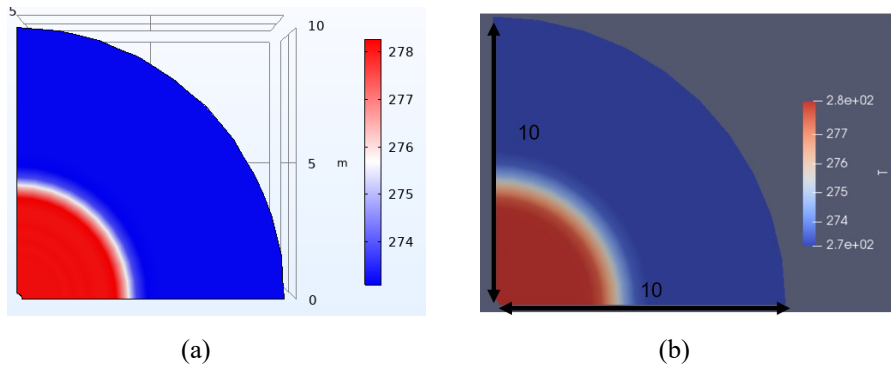


Fig. 9 Simulation results of temperature (K) given by (a) COMSOL (b) deal.II

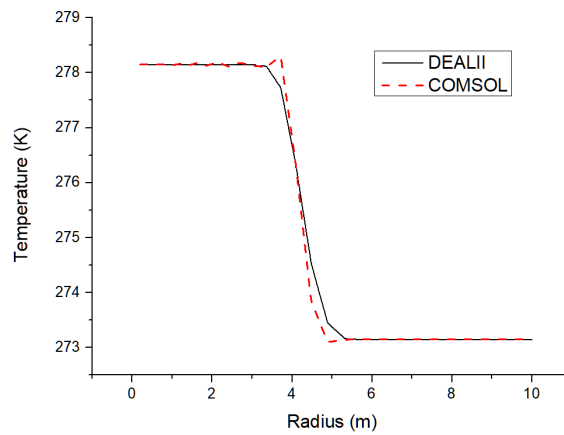


Fig. 10 Temperature distribution in the r direction

A large scale three-layer model is built as shown in **Fig. 11**. The size of the model is 20 m in radius and 300 m in depth. A 6-month hot water injection is simulated. Due to the axisymmetric nature, a small angle is set in the circumferential direction to reduce the scale of the model. There are three formation layers in the model; (i) caprock at the top, (ii) aquifer in the middle, and (iii) basement rock at the bottom. The model parameters are listed in Table 2. The hydraulic conductivity of the aquifer is set to 1×10^{-6} m/s. For the caprock and basement rock, the hydraulic conductivity is set to 1×10^{-10} m/s. and they are recognized as impermeable formations. Hot water of 288.15K is injected into the aquifer from the wellbore.

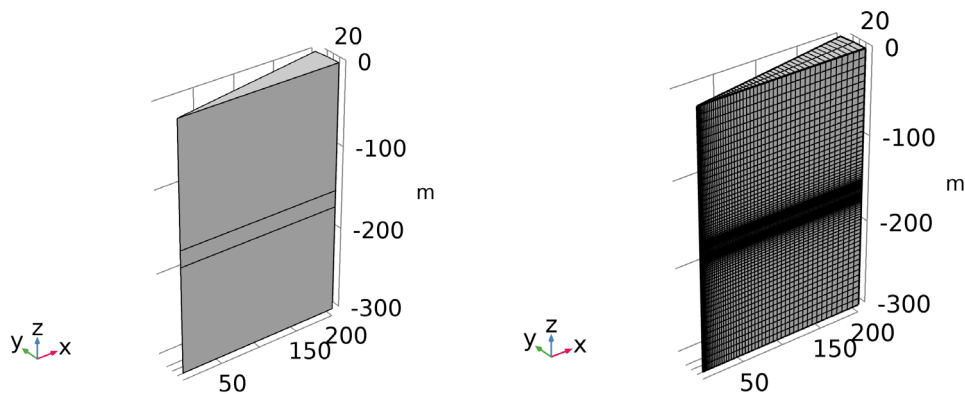
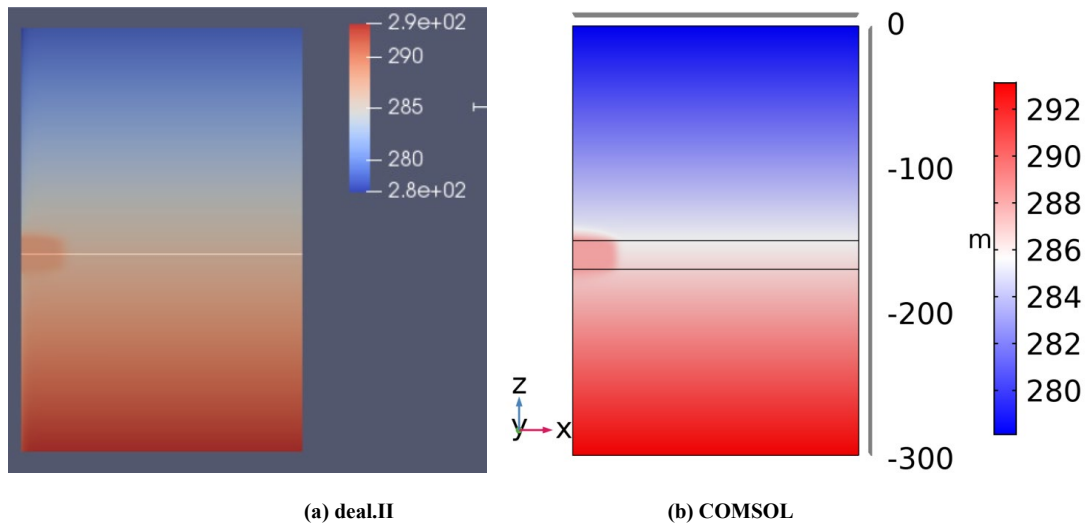


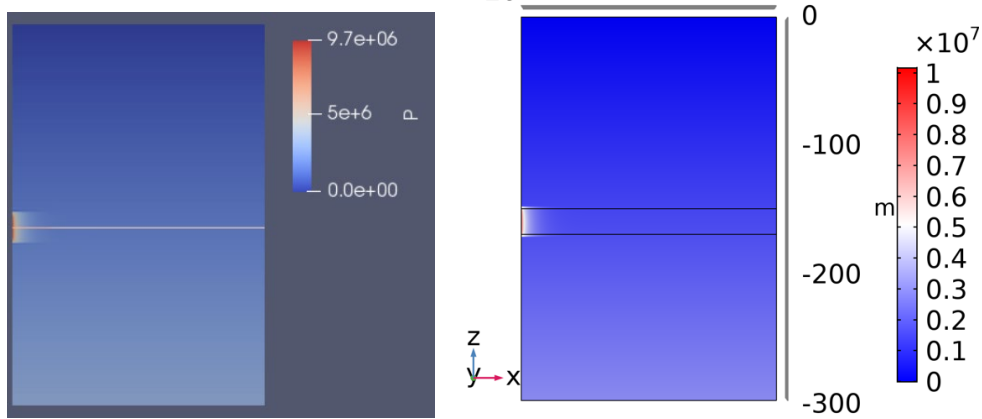
Fig. 11 Geometry and mesh of the model

Table 2 Parameters of materials

Parameter	Value	Unit	Comment
c_T	1.2×10^6	J/K/m ³	Heat capacity for all formations
λ	1.2	W/K/m	Heat conductivity for all formations
B_{poro}	1×10^5	Pa	Porous compressibility
T_{top}	278.15	K	Temperature at the top of model
T_b	288.15	K	Wellbore temperature
P_0	0.1	MPa	Initial pressure
Q_b	0.001	m/s	Injection flux
C_w	1×10^6	J/K/m ³	Heat capacity of water
dT	0.05	K/m	Temperature gradient

The simulation results of the temperature and pressure at 180 days are shown in **Fig. 12** and **Fig. 13**, respectively. Heat flows into the aquifer with water from the wellbore and the temperature of the aquifer increases. Due to the low permeability of the caprock and basement rock, the heat in the vertical direction propagates slower than that in the radial direction. This is due to slow heat convection in the vertical direction. The results given by deal.II and COMSOL yield a similar trend. The temperature and pressure distributions along the centerline of the aquifer are given in **Fig. 14**, whereas those along the wellbore in the vertical direction are shown in **Fig. 15**. The comparisons show that the solutions given by deal.II match well with those computed by COMSOL.

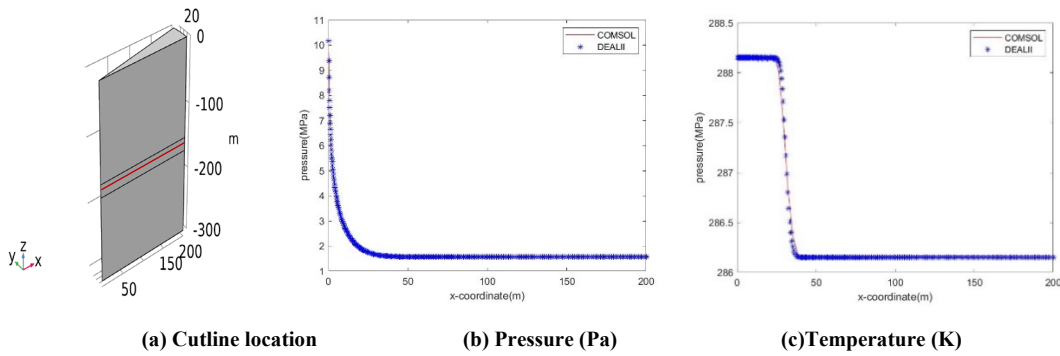
**Fig. 12 Comparison of temperature (K) between deal.II and COMSOL**



(a) deal.II

(b) COMSOL

Fig. 13 Comparison of pressure (Pa) between deal.II and COMSOL

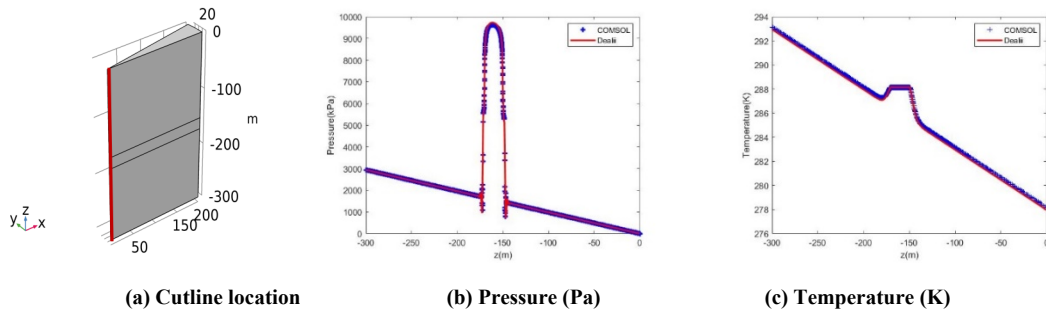


(a) Cutline location

(b) Pressure (Pa)

(c) Temperature (K)

Fig. 14 Comparison of temperature and pressure distribution in the radial direction



(a) Cutline location

(b) Pressure (Pa)

(c) Temperature (K)

Fig. 15 Comparison of temperature and pressure distribution in the vertical direction

5. Parallelization

To conduct a simulation much larger than those shown in the previous section, a parallel scheme needs to be implemented. deal.II offers some open-source wrappers connecting to open source parallel programs such as message passing interface (MPI) and Portable, Extensible Toolkit for Scientific Computation (PETSc). In this section, deal.II PetscWrapper is introduced and the results of simulating a hypothetical operation of a shallow closed-loop geothermal system at Treasure Island are presented.

There are two ways to utilize multi-processor machines: (1) Each machine keeps the entire mesh and

DoF handler locally, but only a share of the global matrix, sparsity pattern, and solution vector is stored on each machine and (2) The mesh and DoF handler are also distributed, i.e., each processor stores only a share of the cells and degrees of freedom. No processor knows the entire mesh, matrix, or solution. Problems solved in this mode are usually large (100s of millions to billions of degrees of freedom) that no processor can or should store even a single solution vector.

5.1 Shared parallelization method

The shared parallelization method can handle the scale of the problem of interest in this study and meanwhile save time for communication between different computing nodes. First, the entire domain is meshed and the mesh is partitioned between processors. The linear system is formed by distributed matrix and vectors processed in different processors using an external parallel programming library PETSc (Balay et. al. 2019). Then, a linear solver given by PETSc is used to solve the linear system. This library can make the assembling and solving in parallel as if everything was processed locally without carrying out the communication between the processors. For a big matrix inverse problem, an iteration method is preferred in place of using the direct solver. For the symmetric matrix solver, the conjugate gradient method is used. For the asymmetric matrix solver, the GMRes method (Saad et. al 1986.) is used.

The existing PETSc Wrappers in deal.II is used to carry out the parallelization rather than using a low-level parallel programming library such as MPI to build the data structure. PETSc provides a data structure to store the distributed matrix and vectors, which are processed by every processor in the MPI network. For the matrix, every processor in the MPI network only stores those rows of the matrix that correspond to DOFs it "owns". For the vectors, they either store only elements that correspond to DOFs the processor owns (this is what is necessary for the right-hand side), or also some additional elements that make sure that every processor has access to the solution components that live on the cells the processor owns (so-called **locally active DOFs**) or also on neighboring cells (so-called **locally relevant DOFs**). The wrappers are used to give PETSc a more modern, object-oriented interface, and to make the use of PETSc and deal.II objects as interchangeable. The main point of using PETSc is that it can run in parallel. At the same time, PETSc also provides dummy MPI stubs, so that it can run on a single machine if PETSc is configured without MPI. (Frohne et al., 2016)

The parallelization scheme is shown in **Fig. 16**. Each process has a complete copy of these objects, and all processes have the exact copies of what the other processes have. Each copy of the triangulation is partitioned or marked on each of the processors. The function `CoupledTH<dim>::make_grid_and_dofs()` is used to ensure which processor owns which cells. The parallel finite element code follows the scheme where every copy of the code runs through the same blocks of the code at the same time. During this time, all processors communicate with each other. The parallelized matrix and vector are assembled for jobs running on an MPI network by calling `CoupledTH<dim>::assemble_system()` function. Then, `CoupledTH<dim>::solve()` solves the local solution vector that stores only a subset of vector entries. Finally, local solutions are combined in one processor, which can be done via the `pcout` function. **Fig. 17** shows an example of the shared parallelization scheme, in which PETSc equally divides the whole mesh into different processors and solve the similar scales of the linear system in balance. Each processor will hold all the grids but only deal with only one part then calculate its own part. As the third level from the top shown in Fig. 17, each processor just calculates one part and gets one part of the solution of the whole model. The colors shown in the figures are the temperature contours given by different processors. The solutions obtained in different processors are then combined to get the whole profile.

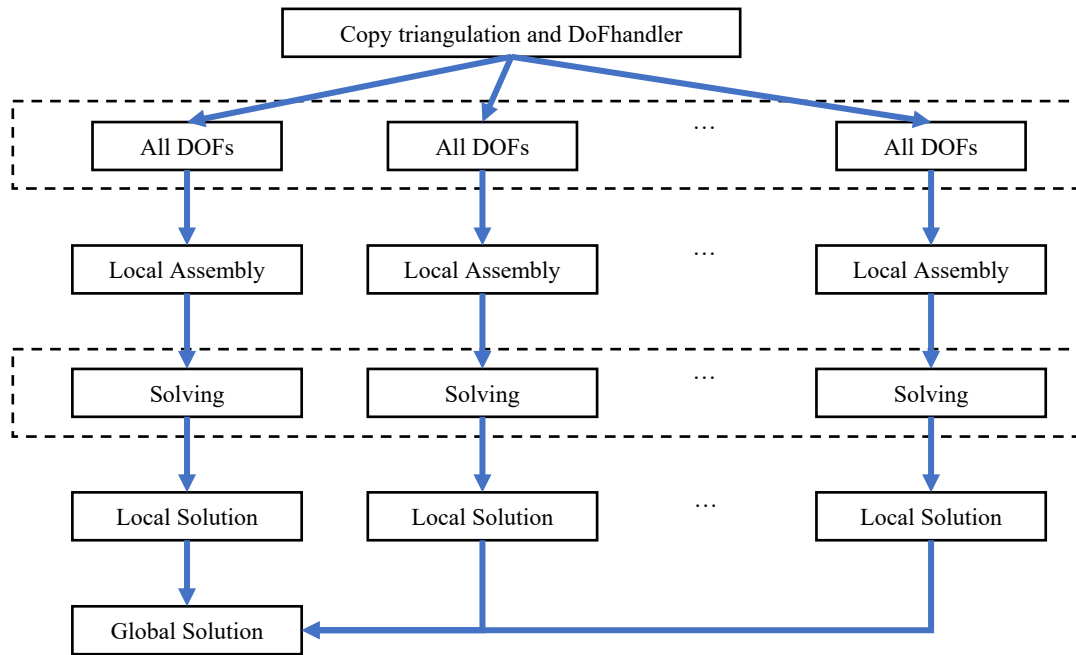


Fig. 16 Shared parallelization scheme

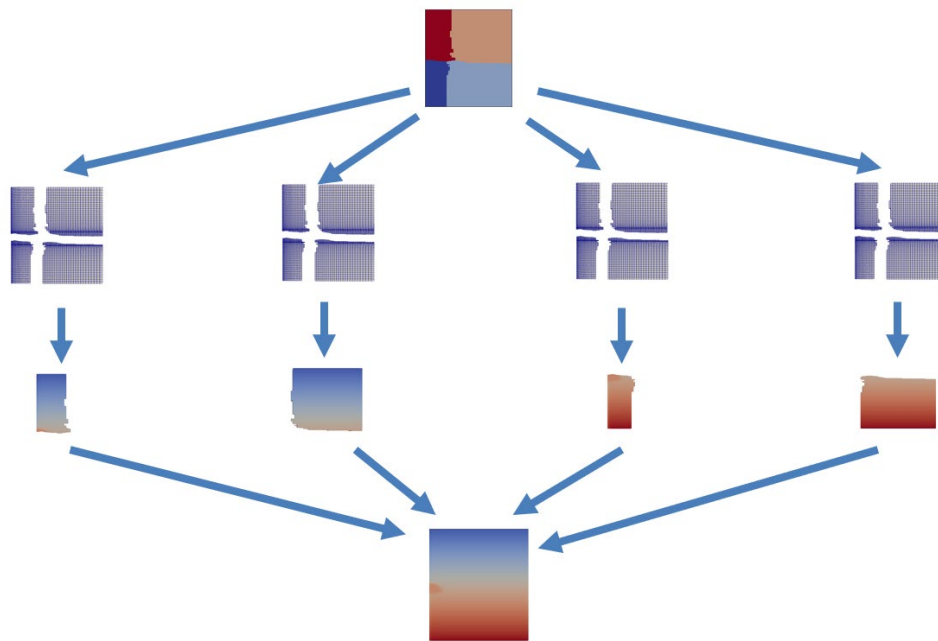


Fig. 17 An example of the shared parallelization scheme in which four parts of whole model marked by different processors are colored and each processor holds all grids but just solves the temperature solution in its own part as shown by rainbow color distribution.

Fig. 18 and Fig. 19 show the comparison of the temperature and pressure profiles using the non-parallelized code and the parallelized code. Both solutions given by these two different codes are the same. Table 3 shows the computation time spent on this example using different computers with different number of processors. On personal computers, the commercial software COMSOL takes more than three times the computation time of that required by the current code for single processor computation. With the increase in the number of processors, COMSOL does not show good improvement in the speed. In

contrast, the current code can speed up by two times when the number of processors doubles. However, when the number of processors increases by more than two, the speed is not improved further. The speed even becomes slower with an increasing number of processors when the number is larger than 4. When a high performance computer is used, the time can be further reduced.

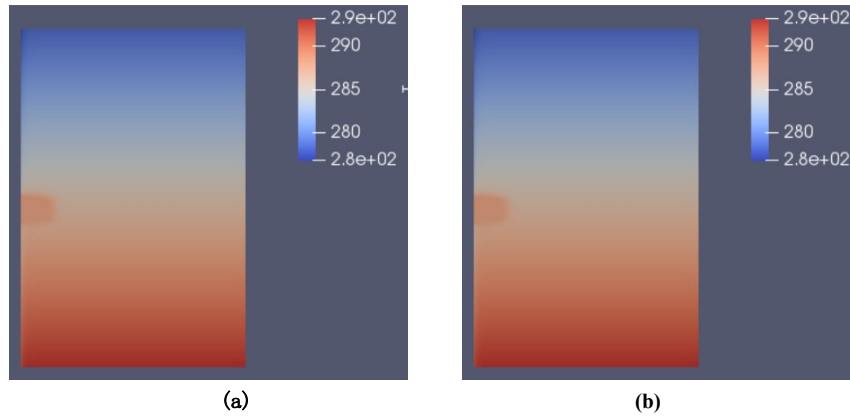


Fig. 18 Subsurface temperature given by (a) non-parallelized code (b) parallelized code

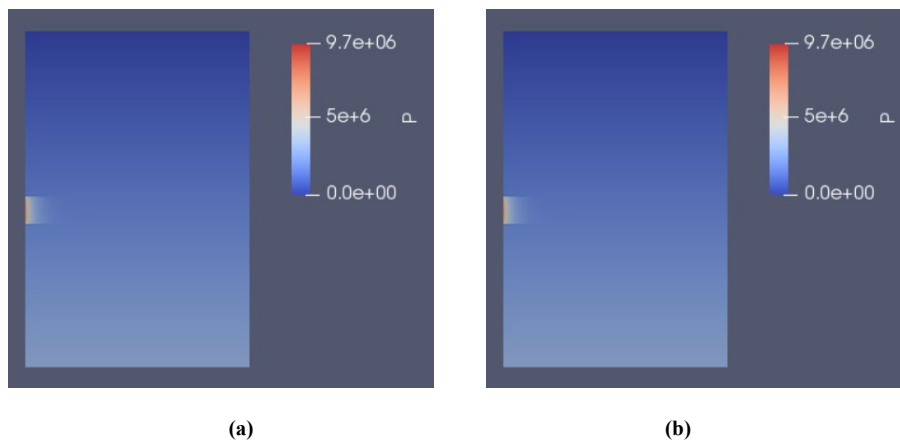


Fig. 19 Subsurface pressure given by (a) non-parallelized code (b) parallelized code

Table 3 Computation time spent on different computers with multiple processors

Num_MPI	COMSOL(PC) i7 8750H	Computation time (PC) i7 8750H	Computation time (HPC 1 node)
1	1553 s	422 s	46 s
2	1284 s	268 s	24 s
4	1230 s	236 s	19 s
6	1496 s	240 s	17 s
8	1502 s	261 s	16 s

5.2 Distributed parallelization method

Another scheme applied in this study is distributed parallelization, in which each processor just deals with its own DOFs. The time for assembling system and vectors is saved because each processor does not need to loop all cells to find out which cells are owned by itself. Meanwhile, each processor does not need to read large amount of memory for all cells. Instead, it just needs to take care of its own cells.

Therefore, compared with the previous shared parallelization method, the distributed parallelization method can save computational time in assembling matrix and vectors and putting into memory. However, because each processor just holds its own cells without any information with others, MPI is needed to obtain the information from other cells. Passing messages also takes time especially when using a large number of processors. Dealii introduces PETSc to help user write in parallelized code, which is easier than coding the message exchanging. The scheme is shown in **Fig. 20** and **Fig. 21**. Different from the share parallelization scheme, one part of the whole grid is passed to each processor in the distributed parallelization scheme. As shown in **Fig. 21**, each processor just holds one part of the grid and deals with its own part. It reduces the usage of memory and the processor can save much time on assembling system because it just needs to traverse the grid passed into itself. Then, like what was done using the shared scheme, each processor processes its own part of the model and gets the solution by solving linear system. Finally, all the solutions given by different processors are combined together and outputted through one processor.

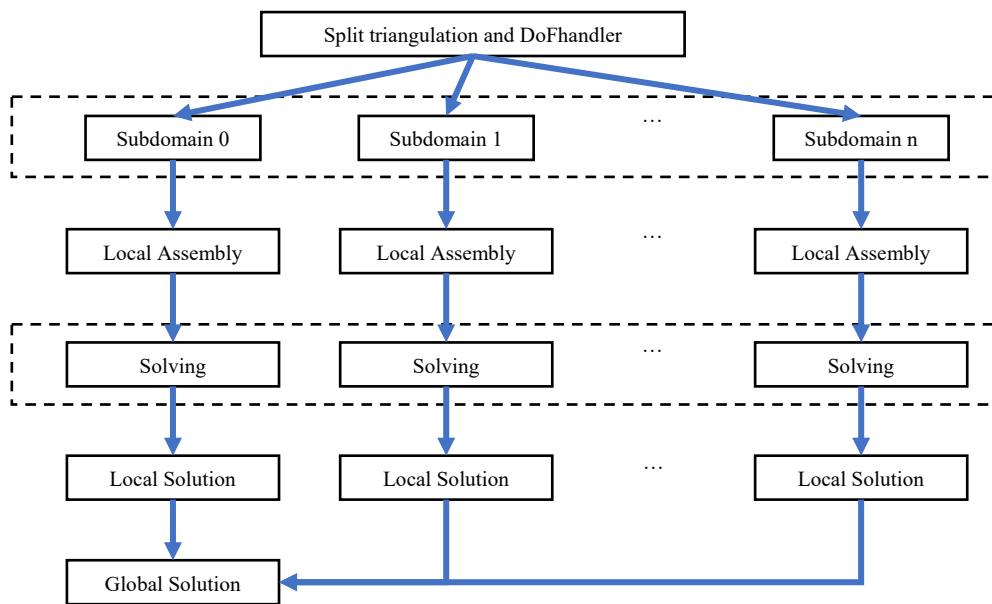


Fig. 20 Distributed parallelization scheme

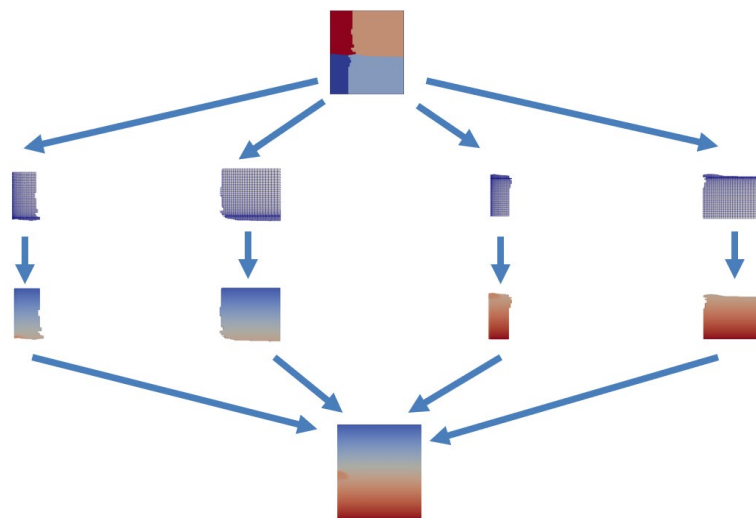


Fig. 21 An example of the distributed parallelization scheme in which four parts of the whole model are passed to

different processors and each processor just holds one part of the whole grids and solves the temperature solution in its own part, as shown by the color contours

Fig. 22 shows that computation time decreases with increasing number of MPI processors using both shared and distributed schemes. It is shown that the distributed parallelization scheme makes the code much faster on assembling system than the shared scheme (compare Fig. 22(a) with Fig. 22 (b)). For solving a linear system, both methods have similar computational speed when the number of processors is large. The relationship between the number of processors and consumed time in assembling systems and solving system processes yields a similar linear relationship in log-log coordinate. However, the shared scheme only reduces a little in the time consumed in assembling the system as the number of processors increases. As shown in Fig. 22(c), from the single processor to dual processors, the computation time using the shared scheme decreases by half. When the number is larger than 4, the magnitude of computational time reduction becomes smaller because the operation of assembling the matrix takes more time than solving the linear system. Meanwhile, with the increasing number of processors, more time is spent on message passing. As shown in Fig. 22(d), the message passing blocks the improvement of performance when the number of processors is larger than 8. So, if the scale of the problem is large enough, the time consumed in message passing will become valuable. The efficiency of the code for a larger problem is shown later on in the Treasure Island case study.

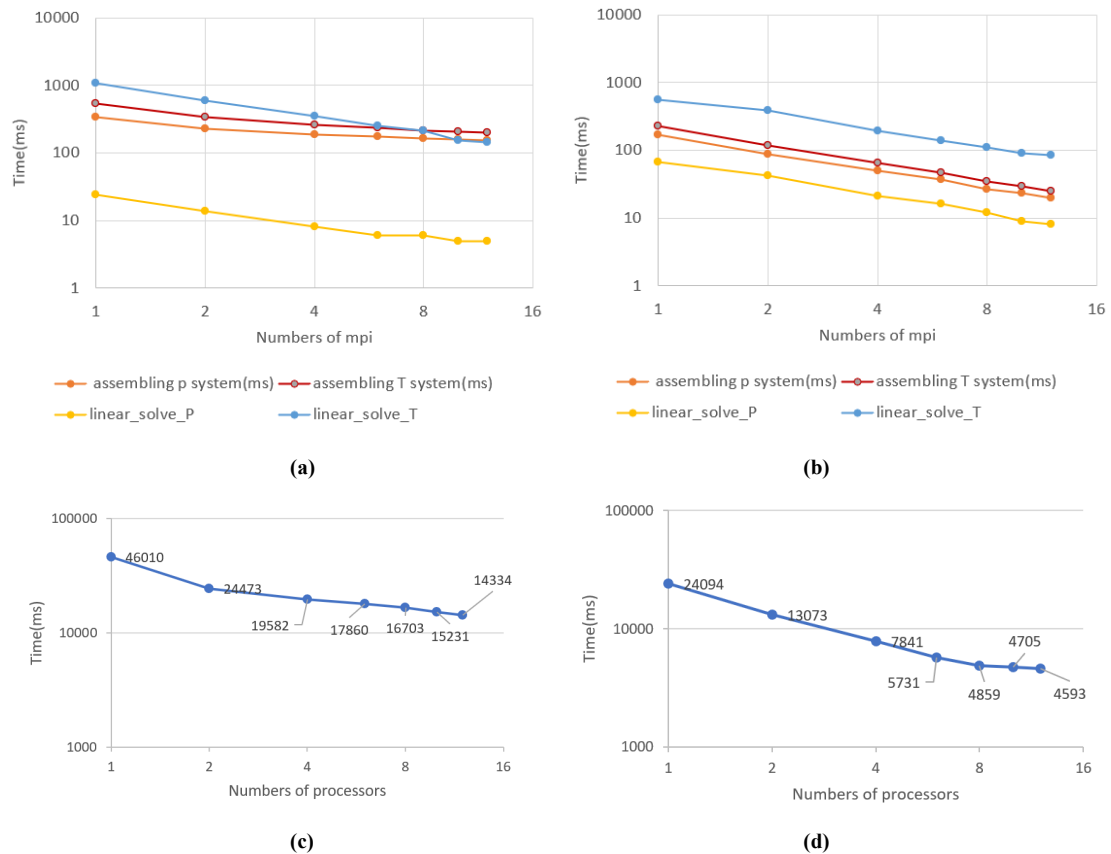


Fig. 22 Time consumption with increasing number of processors including (a) time consumption by different computation processes such as assembling system and solving system using shared parallelization scheme; (b) total time consumption using shared parallelization scheme (c) time consumption by different computation processes such as assembling system and solving system using distributed parallelization scheme; (d) total time consumption using distributed parallelization scheme

6 Treasure Island case study

6.1 Introduction

Treasure Island is a man-made artificial island which was constructed in 1936-1937 by hydraulic filling behind a perimeter dike. Being initially planned to serve as an airport for Pan American Airline's Pacific Rim flying boat service, it became part of the Treasure Island Naval Base during WWII. In 1996, Treasure Island was decommissioned by the Navy and opened for public use and development. Today, it is a part of District 6 of the City and County of San Francisco.

The Treasure Island redevelopment project consists of the construction and management of new community facilities on San Francisco Bay Area's Treasure Island and Yerba Buena Island (**Fig. 23**). Treasure Island is a man-made island while Yerba Buena Island is a naturally occurring one that is connected to Treasure Island with a causeway. The current redevelopment plan consists of mixed-use residential and commercial area. As shown in **Fig. 24**, the proposed residential diversity of the Treasure Island site includes the integration of mid-rise buildings with high-rises. Townhomes and stack flats are also major components of this new development project. Further details of the redevelopment are given in Appendix A.

Since there are multiple types of buildings that are planned to cover a major portion of Treasure Island, their energy needs are also one of the concerns of the project developers. Application of the state-of-the-art and clean energy production systems that have the capability of meeting the energy demands of the whole Island community has been considered. The usage of district-scale ground source heat pump system was considered as a possibility ([City and County of San Francisco Urban Ground Source Heat Pumps – Phase I](#)) and this study considers this hypothetical implementation as a case study.



Fig. 23 Treasure Island and Yerba Buena Island (ENGE0 Inc 2009)



Fig. 24 The Treasure Island Redevelopment Project (ENGEIO Inc 2009)

6.2 Geology

A comprehensive literature review for publications regarding Treasure Island's geology and geotechnical properties has been conducted. Lee et al. (1969) describe that the Treasure Island fill was placed upon Yerba Buena Shoals with a shallow water area in excess of 735 acres. In the direction of the northwest point of Yerba Buena Island, a small portion of the fill area is sand spit. The above-water area of the fill is about 400 acres, with a width of 1040 m and a length of 1682 m. The fill used for the construction of Treasure Island was composed of 65% fine to coarse loose sand and 35% soft mud. Lee et al. (1969) state a noteworthy incident during the construction of the island as follows: "Following the completion of the east sea wall, a section of 152 m long suddenly settled 3-5 m and disappeared from the sight. As a precaution, the construction plans were modified by flattening the side slopes of the wall and depositing a mattress of heavy sand on the bottom beyond the toe of the slope to act as a counter-weight and prevent the underlying plastic mud from heaving and thus resulting in additional settlement in the fill".

Andrus et al. (1998) used spectral analysis of the surface waves method for profiling the south-eastern corner of the island, which is also designated as an Improved Soil Area. The recorded shear wave velocities are presented for the first 20 m. The authors observed that the first 12 m of Treasure Island fill is sand, with samples above a depth of 6 m contain as much as 17 % fines. Beneath the sand fill, 3 m of native silty clayey sand followed by 27 m of soft to stiff clay with interbedded sand layers have been recorded. Sandstone and shale bedrock are reported to occur at a depth of 87 m, while the water table is about 2 m below the ground surface.

Baise et al. (2003) installed a deep instrumentation array through the soil to the bedrock in order to collect information on site response. The soil profile presented in this study is consistent with the results from Andrus et al. (1998). One upside of this study is the presentation of shear wave velocities up to 110 m from the ground surface. According to this soil profile, the first 12 m is composed of artificial fill, where Holocene Bay sediments were observed to a depth to 40 m. Between depths of 40 m and 90 m, Pleistocene Bay sediments were recorded. The same study concludes that the top of the Franciscan bedrock is encountered at a depth around 90 m.

One of the most comprehensive soil profiling for Treasure Island is presented in Power et al. (1998). Soil profiles are provided for varying depths of 70-100 m. Comprehensive soil profile cross sections are provided both for the transverse and longitudinal directions of Treasure Island. While the underground

profile data is consistent with the other studies for Treasure Island, Power et al. (1998) also include the Standard Penetration Test (SPT) data up to a depth of 18.3 m. SPT data can be utilized as a reference check mark for comparing it with the laboratory test results from ENGE0. Further details of the geology in and around Treasure Island are given in Appendix B.

6.3 Shallow Closed-looped Geothermal Energy piles

Ground Source Heat Pumps (GSHPs) provide sustainable heating and cooling energy for housing, offices and retail spaces. For new building and underground developments, it is possible to incorporate the primary heat exchangers through the foundation elements (e.g., piles and basement walls) or into the tunnel linings. They are called energy (or thermal) piles/walls/tunnels.

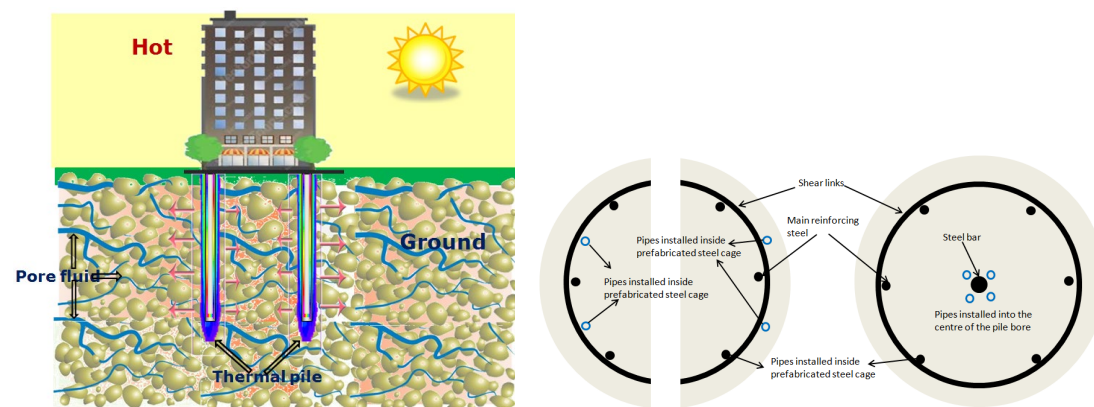


Fig. 25 Heat transfer of thermal pile (Soga and Rui, 2016)

In an energy pile system, the heat exchanger pipe network is installed in the structural piles of a building as shown in Fig. 25. Heat exchanger pipes are attached to the reinforcement cage of the pile before concrete is poured to create the pile, as shown in Fig. 26. As concrete has excellent thermal conductivity and good heat storage properties, foundation piles are an ideal medium for heat transfer into the surrounding ground. In their early years, energy piles were mainly built as driven precast concrete piles with integrated heat exchange tubes. The technology has been extended to large-diameter deep bored piles, which allow for placing multiple U-shaped loops of pipes used to circulate the carrier fluid. In bored energy piles, the pipes are made of high-density polyethylene and are 20-25 mm in diameter and about 2 mm thick. They are fixed to the reinforcement cage, as shown in Fig. 25. A heat carrier fluid used in the primary circuit is water, saline solutions or water-glycol mixtures. The latter mixtures have proven to be the most suitable option because they have good antifreeze properties and low environmental impact. The fluid flow rates and pipe diameters are selected to achieve turbulent flow conditions, so that heat transfer can be enhanced.

The overall thermal performance of the energy pile depends on the position of the pipes within the pile as well as the size of the concrete part of the pile in relation to the size of the pipes. When designing energy piles, such differences between energy piles and GSHP borehole exchangers as well as the variation in pipe positions and numbers need to be considered.

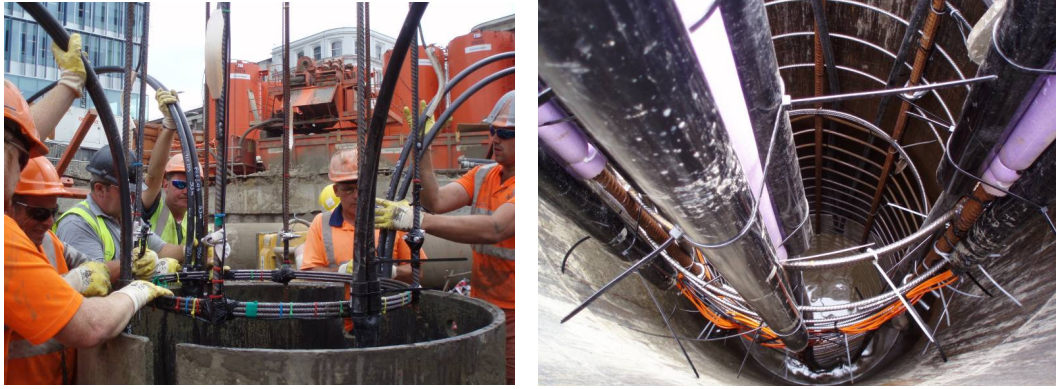


Fig. 26 Installation of geothermal loop into the energy pile (courtesy of Kenichi Soga)

The first well-documented energy piles were installed in Austria in 1984 (Brandl, 2006). Since the mid-1980s, energy piles have found application across Northern Europe (e.g. Suckling & Smith, 2002; Brandl, 2006; Adam & Markiewicz, 2009). In the UK, there have been a number of energy pile schemes constructed such as the ‘One New Change’ project (Garber et al., 2013b), as well as many smaller projects such as Keble College (Suckling & Smith, 2002) and Lambeth College (Bourne-Webb et al., 2009). Brandl (2006) describes the first well-documented energy wall installation in Switzerland in 1996. In the UK, the first energy wall was installed at the Bulgari Hotel in London in 2010 (Amis et al., 2010), triggering the implementation of such systems in other high-profile projects such as the Crossrail tunnel project (Nicholson et al., 2013).

In this study, it is considered that a series of energy piles are installed at the footprint area where the new buildings are planned to be constructed as shown in Fig. 24. A total of 1130 energy piles were integrated into the model and their locations are shown in Fig. 27 (a).

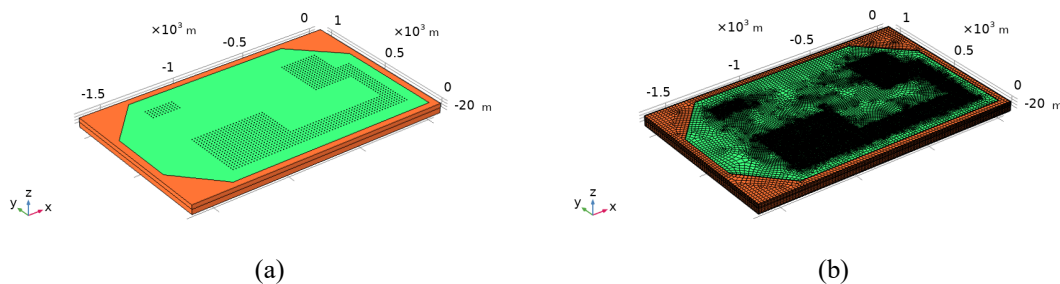


Fig. 27 Treasure Island modeling (a) geometry model in which the dots are the locations where energy piles are installed and (b) mesh, which is dense around the piles and coarse around far-end boundary

6.4 Finite element model

The performance of energy piles coupled with a closed looped ground source heat pump system are simulated in this study. As shown in Fig. 27(a), the length of the island in x-direction is 1680 m. The width of the island in y-direction is 1040 m. The depth of the island in z-direction is 100 m. The whole island area is around 400 acres. From the edge of the island to the boundary of the whole model, the area of 45.7 m in width is extended to simulate the sea bed close to the island. Since the depth of the seabed is around 6.1 m, which is small relative to the model depth, this depth difference is not modeled. It is assumed that the part of the island submerged below the sea-level for a long period of time has the same

temperature of 287.45 K as the sea. The temperature of the island above sea level is given as model input (constant or seasonal changes).

A series of energy piles are set beneath the buildings as shown in **Fig. 27(a)**. The spacing between the piles is 20 m. The radius of the piles is 0.75 m and the length is 60 m. In total, there are 1130 piles in the simulation model. **Fig. 27(b)** shows a fine mesh around the piles and a coarse mesh far from the piles. The number of DOFs is 1,301,718.

For the underground geology, starting from the ground, the hydraulic fill was placed during the initial construction of the island. Beneath the hydraulically placed fill, a thin layer of sand-shoal deposits is observed. Young Bay mud lies beneath the sand-shoal deposits. Old Bay deposits, which are mainly composed of clay, are overlain by the Young Bay mud. At the bottom of the underground profile, there exists Franciscan rock formation. Depending on the location, the Franciscan rock formation is observed at a depth of 70-80 m beneath the ground surface throughout the island. Running the developed three-dimensional model requires the input of hydrothermal properties of the corresponding soil types. Thermal properties for the soil types observed in Treasure Island has not been extensively studied and hence values in literature for this location were not found. It is expected that the geotechnical consulting partner will run tests on the soil samples collected from the island in order to calculate the hydrothermal properties.

The shoal deposits on the island are classified as silty to clayey sand (ENGEО Inc., 2019). For those sand deposits encountered on the island, Misra et al.'s (1995) study is also taken as the reference for calculating the thermal conductivity value through the use of proposed empirical relationships. Heat capacity for sand is obtained from Russo and Civita's (2009) work involving clayey sand in the development of open-loop groundwater heat pumps for large buildings. For the hydraulic conductivity of sandy shoal deposits, values from Phillips' (1993) study on the groundwater in San Francisco is adopted.

In order to assign the hydrothermal properties of soils in the three-dimensional model, a literature review has been performed to assign representative values for similar materials. The soil descriptions provided by ENGEО Inc. (2019) are used as the benchmark for obtaining the hydrothermal properties of similar soils. Young bay deposits are described as medium-stiff fat to lean, normally consolidated clays with interbedded lenses of silty and clayey sand. The thermal properties for Young Bay mud are referenced from Goto et al. (2017). Nguyen's (2006) study on Bay Mud is utilized for adopting the hydraulic conductivity value of both Young Bay mud and Old Bay deposits.

ENGEО Inc. (2019) describes the Old Bay deposits as interbedded stiff to hard, low to bluish-gray to greenish-gray high plasticity clays, dense to hard fine silty and clayey sands. Misra et al. (1995) developed a theoretical model for predicting the thermal conductivity of an ideal soil mainly based on the degree of saturation of the soil, which is taken as the reference study for the thermal conductivity value evaluation for old bay deposits. The Old Bay deposit's heat capacity value is taken from Goto et al. (2017), which focused on the thermal properties of mud-dominant marine sediments that share a similar classification with the Old Bay deposits.

The Franciscan Formation bedrock encountered in deep borings across the Island consists of dense, weathered dark gray sandstone and shale. For that formation, Konakova (2013)'s dataset for thermal properties of various sandstones is adopted for the heat capacity value of Franciscan Formation. Walters et. al. (1991) investigated Franciscan graywacke thermal conductivity value based on mean of 563 measurements of samples near The Geysers geothermal field. Well tests indicate that these rocks have fracture network permeabilities of 5×10^{-15} to $1 \times 10^{-13} \text{ m}^2$ (Williamson, 1992) – the fracture values would be more appropriate values to use for this model.

The hydrothermal properties gathered from the literature are summarized in Table 4.

Table 4 Parameters of the material of Treasure Island

Soil/Rock type	Hydraulic conductivity (m/s)	Heat Capacity (J/m ³ K)	Thermal conductivity (W/m•K)
Fill	1.1×10^{-5} *	2.5×10^6 #	2.2 ^s
Shoal	3.5×10^{-5} **	2.5×10^6 #	2.2 ^s
Young bay mud	1.7×10^{-9} ***	3.5×10^6 ###	1.5 ^s
Old bay mud	1.7×10^{-9} ***	3.5×10^6 ##	1.7 ^s
Franciscan bedrock	1×10^{-6} ****	2×10^6 ###	2.97 ^{ss}

* Ashford and Rollins. (2002), ** Phillips et al. (1993), *** Nguyen (2006), **** Williamson (1991), # Russo et. al., (2009), ## Goto et al. (2017), ### Konakova, 2013, ^s Misra et al. (1995), ^{ss} Walters et. al., (1991)

The seasonal air temperature variation of Treasure Island is shown in Fig. 28. It is adopted from the U.S. National Weather Service and the weather data is reported for San Francisco International Airport between 1985-2015. The distance between San Francisco International Airport and Treasure Island is about 14 km and hence it was assumed that the seasonal temperature values for the airport can be used as the same for the Treasure Island shallow geothermal energy model. The average temperature in the whole year is 287.45 K. Due to the lack of ground surface temperature, the sunlight strength and local humidity records for the island, the air temperature record is assigned as the ground surface temperature.

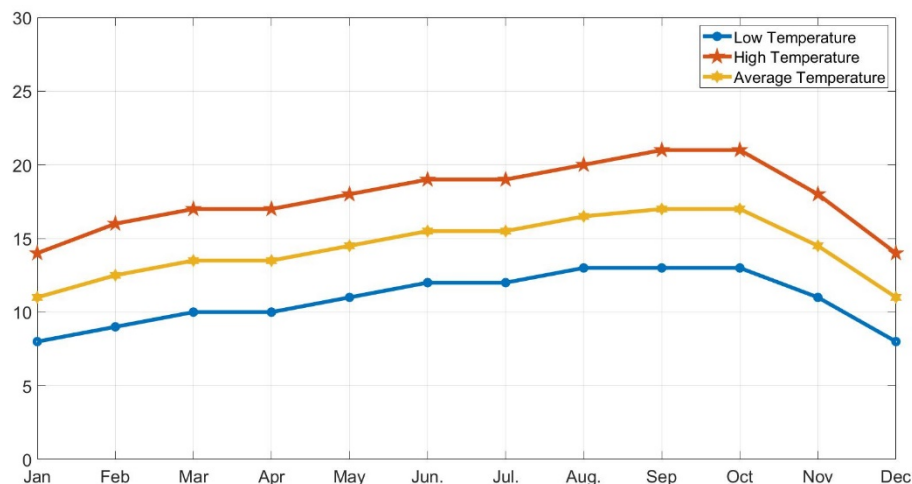
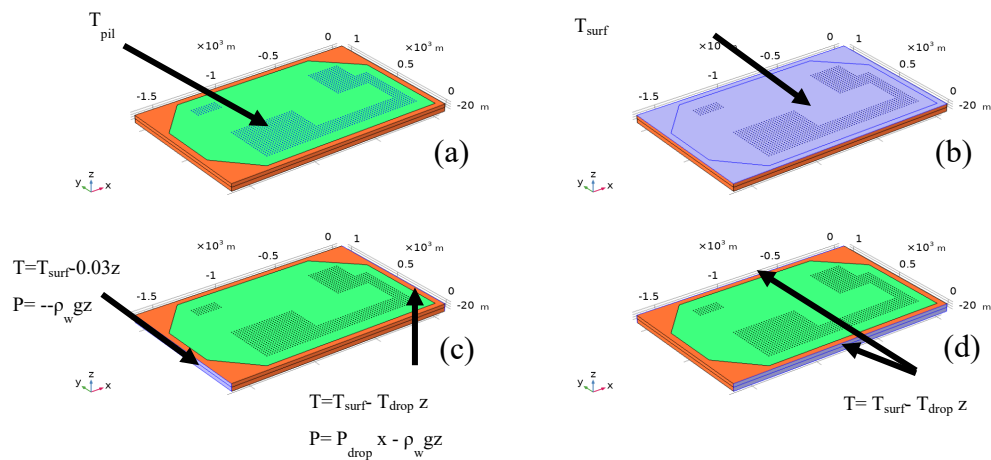


Fig. 28 Air temperature variation of San Francisco International Airport from the U.S. National Weather Service) which is used as the ground surface temperature of Treasure Island

In this study, three cases are used to investigate the effects of underground heat convection and seasonal heat injection and extraction on the subsurface temperature distribution using the new HPC code. In CASE 1, the temperature at the top surface is set to the average value of the whole year. The surface temperature is consistent with its initial state, which is equal to 287.45K. The temperature gradient T_{drop} is assembled to be 0.03K/m by assigning a constant flux at the bottom boundary. A heat flux q_T of 0.89W/m², which is equal to the thermal conductivity times the temperature gradient around the bottom bedrock is applied. For the initial pressure distribution, the pressure values on the left-side boundary are assigned as hydrostatic from the ground surface, assuming the water table is at the top boundary surface. On the right-side boundary, the pressure value is assigned to be the sum of 8.5 kPa and the hydrostatic pressure, giving a hydraulic gradient P_{drop} of 5 Pa/m from the right boundary to the left boundary. The boundary conditions are consistent with the initial conditions, which are shown in **Fig. 29**. The pile temperature T_{pile} is set to the average value of the initial underground temperature distributed along the pile plus 13 K, which is equal to 301.35K.

In CASE 2, a pressure gradient of 5 Pa/m is also applied to simulate the convection effects. However, different from CASE 1, CASE 2 assumes the hydraulic conductivity of the shoal sandy formations to be hundred times higher than the listed value in **Table 4**. This is because the contents of silt, clay and fine sand in the shoal formations are variable and the hydraulic conductivity is dependent on the contents. To simulate an extreme situation and gain an obvious convection effect, the hydraulic conductivity is magnified by hundred times. The other initial and boundary conditions are the same as CASE 1.

In CASE 3, different from CASE 1, a relatively realistic surface temperature variation, which is an average temperature monthly in **Fig. 28**, is applied on the top surface of the model. The heat flux from the bottom of the model remains as 0.89W/m². For the convenience of the simulation, the temperature record in May, which is equal to 287.65K and approximates the average temperature yearly, is chosen as the beginning of the simulation so that the results of CASE 1 can be compared to those of CASE 3. Meanwhile, the initial pile temperature is set to the average value of the initial underground temperature distributed along the pile, which equals 288.55K. The variation of the pile temperature is assumed to be a square wave of which the magnitude equals 13 K. This corresponds to a constant value of 301.55K for 6 months during summer and then a constant value of 275.55K for 6 months during winter.



Boundary conditions (a) at the piles; (b) on the top of the model; (c) on the right and left side of the model; (d) on the

front and back of the model

Fig. 30 and **Fig. 31** show the steady-state pressure distribution between the left and right boundaries for CASE-1 and CASE-2, respectively. Both have the same pressure profile with a gradient of 5 Pa/m between the two boundaries. **Fig. 32** and **Fig. 33** show the temperature distributions after 180 days of heat injection at selected locations in CASE-1 and 2, respectively. In the high permeability regions (the upper 10-16 m layers in CASE-2), the heat applied from the piles is carried by groundwater flow and moves toward the left boundary. In CASE-1, due to small groundwater flow, the heat migration in the ground is diffusion dominated. In CASE-2, due to large groundwater flow due to the high permeability, the heat migration in the large permeable layer becomes advection dominated. The heat propagates from the piles toward the left direction driven by the groundwater flow in CASE-2. There is limited heat movement in the underlying low permeability clay layers.

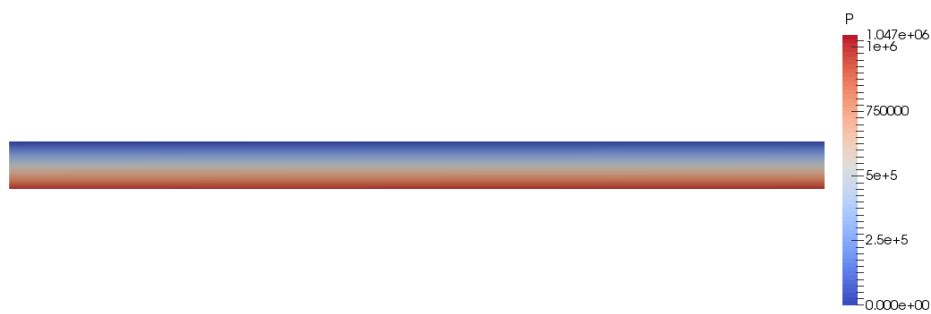


Fig. 30 Pressure distribution in the x-z plane for CASE 1

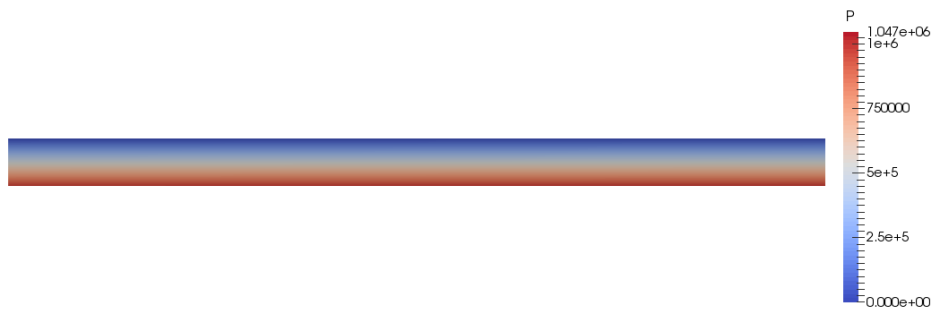


Fig. 31 Pressure distribution in the x-z plane for CASE 2

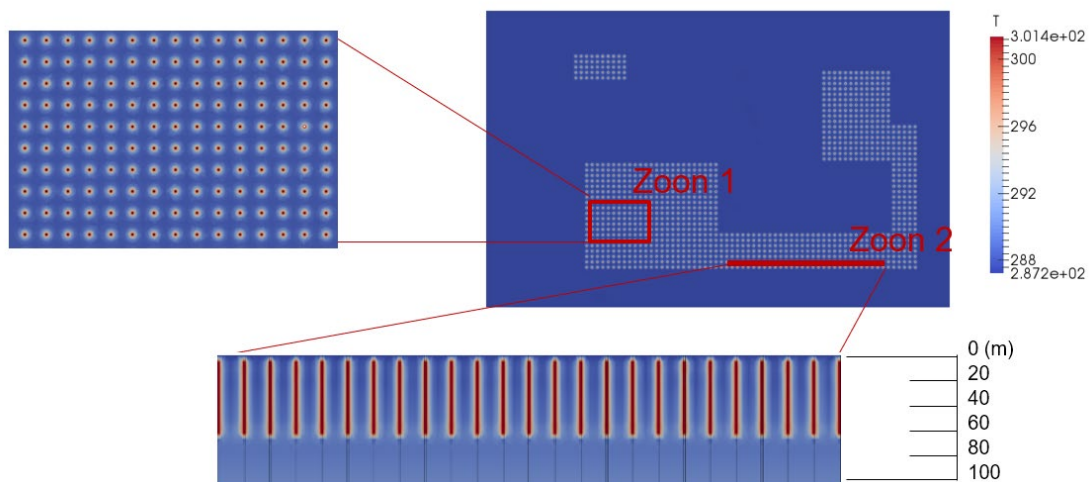


Fig. 32 Temperature distribution after 180 days as a result of heating by piles under the condition of slow subsurface

water flow – CASE 1

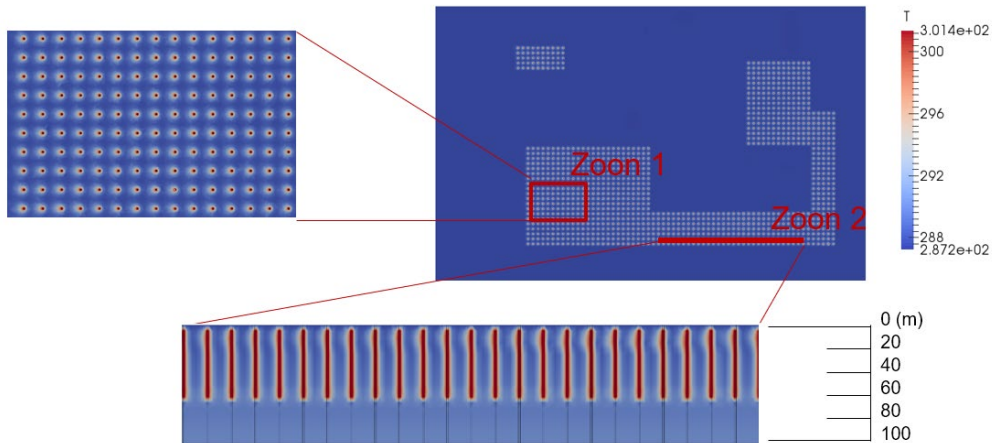


Fig. 33 Temperature distribution after 180 days as a result of heating by piles under the condition of fast subsurface water flow – CASE 2

Fig. 34 shows the variation of underground temperatures at different times of a year for CASE 3. Due to slow groundwater flow, the heat migration in the ground is diffusion dominated. During the first 180 days, the underground temperature is increasing with heat diffusion from the piles. After 180 days, the cooling phase begins and the ground temperature around the piles decreases and the cooling fronts propagate into the soil.

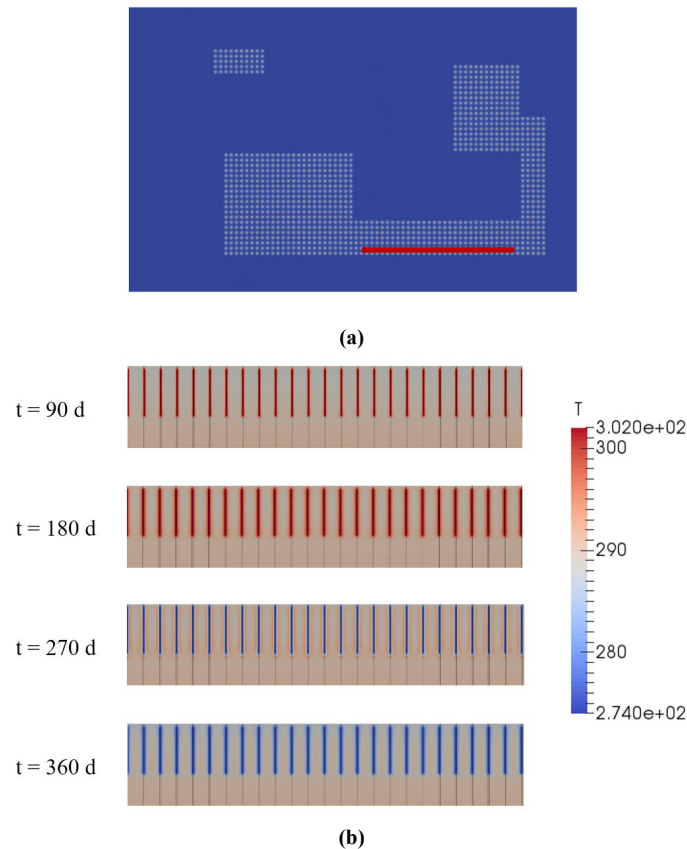


Fig. 34 Underground temperature variation (b) during the cyclic heating and cooling at the cross-section marked as red

line on the island map (a) – CASE 3

The observation lines shown in **Fig. 35** are selected to investigate the details of ground response to thermal loading by both the seasonal ground surface temperature variation and the heating and cooling of the energy piles. The observation lines O-1, O-2 and O-3 are set at the locations of 1 m, 5 m and 10 m away from the left pile, respectively. Because the underground temperature response profile is symmetric with respect to the center at the distance between two piles, it is not necessary to plot the right side of the center line Q-3. To investigate the temperature distribution in the horizontal direction, the observation lines Q-4, Q-5 and Q-6 are set at the location where the temperature responses are representative. For example, Q-4 is at 6 m depth from the surface because the temperature response here is impacted by both ground surface temperature variation and pile heating. Q-5 is at 40 m depth from the surface because this place is at the middle of where the underground temperature is impacted by the pile heating and cooling. Q-6 is at 60 m depth and is at the bottom of the pile with heat propagation into the bedrock.

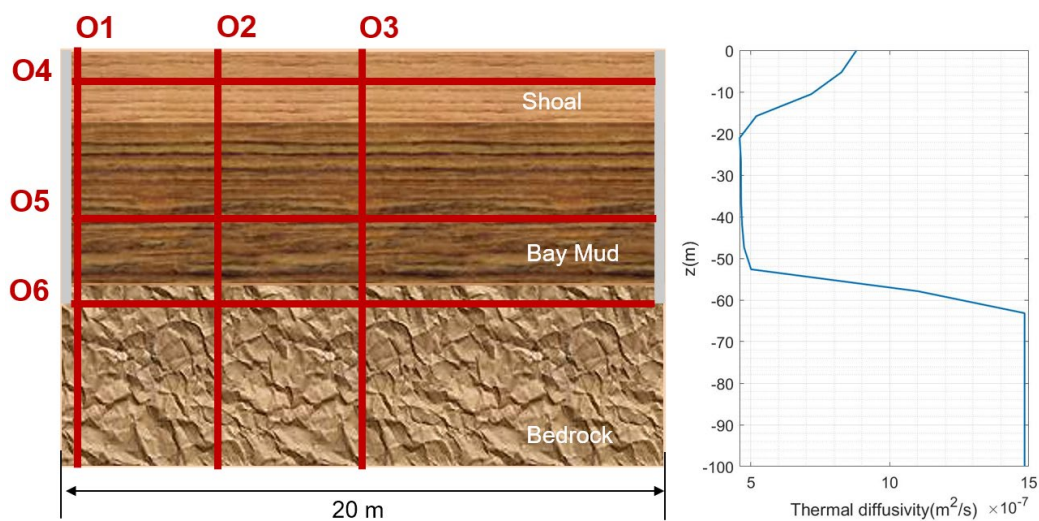


Fig. 35 Heat diffusivities corresponding to different layers and the observation locations in CASE-3

Fig. 36 shows the temperature distributions after 90, 180, 270 and 360 days of heating (for 6 months) and then cooling (for 6 months) at the observation lines O-1, O-2 and O-3. Since heat conduction dominates the underground temperature response, the distribution of underground heat diffusivity plotted in **Fig. 35** is the key factor of impacting the underground temperature profile. The variation of temperature at shallow depths is sensitive to the surface temperature change as shown by comparing **Fig. 35** and **Fig. 36**. However, the seasonal variation only affects the highly heat conductive layers including the filled and shoal formations. It has little impact on the low heat conductive clay layers. The clay layers are mainly affected by the heat injection from the energy piles.

Due to the low heat diffusivity, the injected heat takes a long time to reach to the observation location far from the piles as shown in **Fig. 36(b)** and **Fig. 36(c)**. The underground temperature response at the vicinity of the piles is sensitive to the heat injection as shown in **Fig. 36(a)**. With the increase in the distance from the piles, the impact of heating and cooling on the underground temperature response becomes smaller. This is also observed in **Fig. 37**. Although the pile temperature is decreasing, the temperature at the observation location Q-2 can be increasing due to the residual heating. The temperature at the observation location Q-3 has little change as it is far away from the piles, illustrating

that the interaction of thermal loadings from the two adjacent energy piles is limited in this particular case. The temperature of the bed rock at the depth of 60 m changes faster than the clay layers with heating and cooling due to the high heat diffusivity of the bedrock as shown by comparing **Fig. 37(b)** and **Fig. 37(c)**.

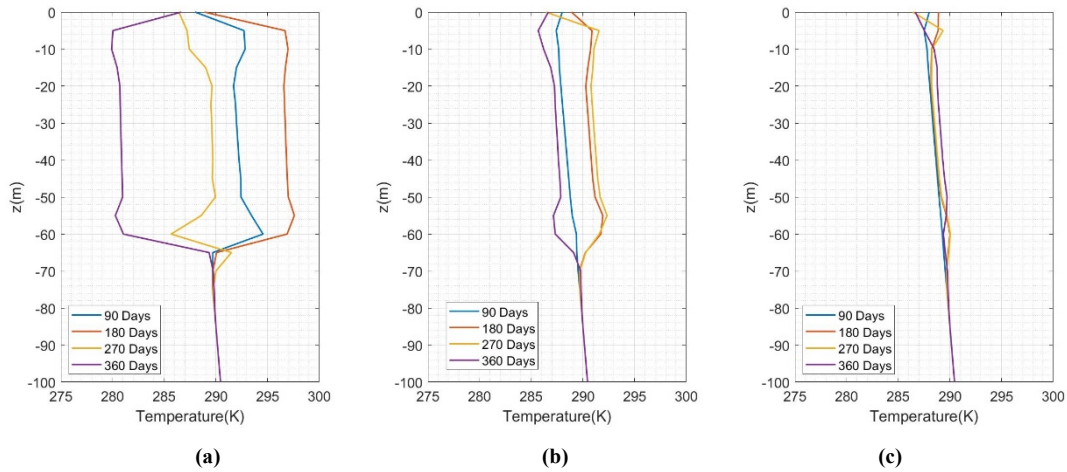


Fig. 36 Vertical subsurface temperature change (in z direction) with cyclic heat injection at the observation locations (a) O-1: 1 m, (b) O-2: 5 m and (c) O-3: 10 m far away from the left pile, respectively

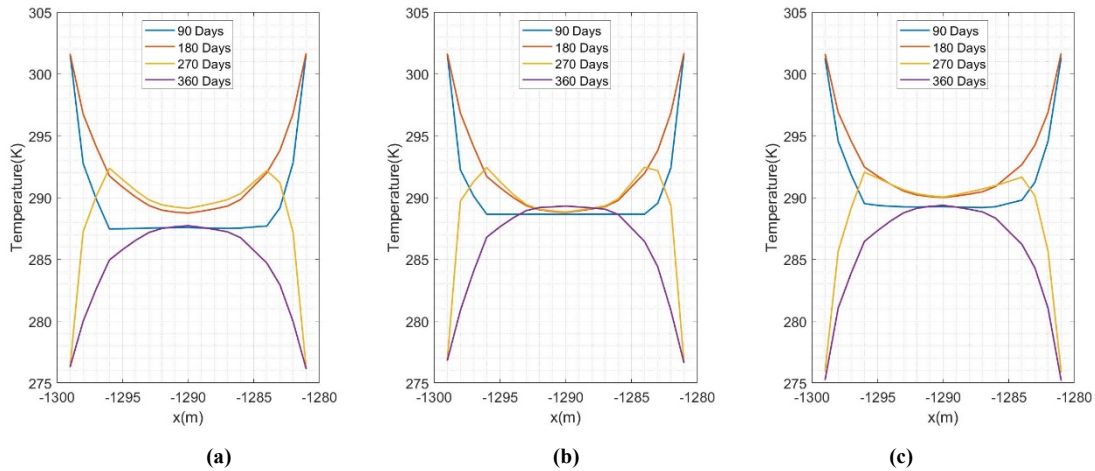


Fig. 37 Lateral subsurface temperature variation between two piles (in x direction) with cyclic heat injection at the observation locations (a) O-4: 6 meters, (b) O-5: 40 meters and (c) O-6: 60 meters depths, respectively

The computational efficiency of the code for this Treasure Island problem is examined. **Fig. 38 (a)** shows the computational time taken by different computing processes including assembling T system, assembling P system, solving T system and solving P system. Most of the computational time is taken to assemble the linear system. The total time spent on the Treasure Island simulation case decreases linearly with the number of the processors in the double logarithm scale as shown in **Fig. 38(b)**. However, with the increase in the number of the processors, the efficiency increases proportionally in the double log scale. For example, using 12 processors, it took 703 seconds to solve a problem with a number of DOFs of 1,301,718. For the smaller problem (283,810 DOFs) shown in **Fig. 22**, most of the computing time was spent on solving the heat equation. However, in the Treasure Island case, the time spent on solving

the heat equation was less than the other processes. This illustrates that, as the model scale increases, assembling the matrix becomes the main time-consuming process due to traversing a large number of cells in the model. Results of this study show that, given the relatively short computing times using multiple processors, multiple scenarios can be explored for the Treasure Island case in a reasonable amount of time.

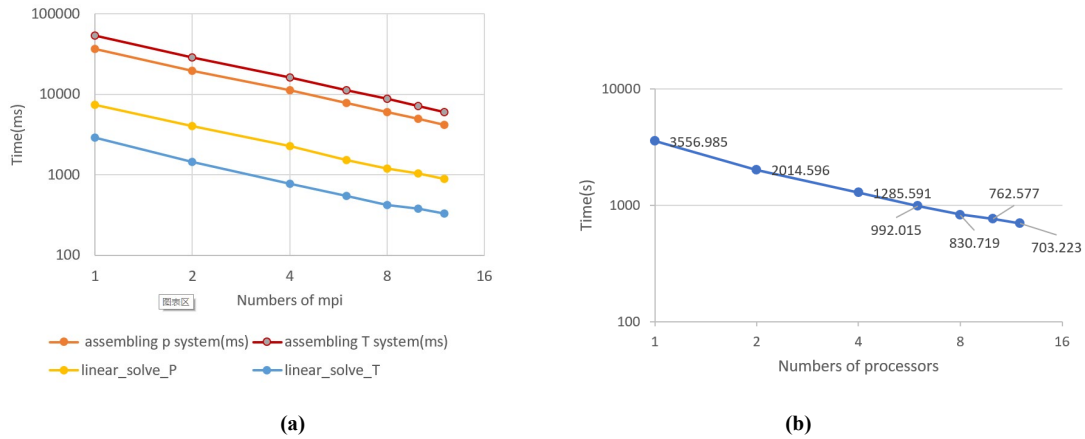


Fig. 38 The effect of the number of processors on computational time for the Treasure Island problem

7 Conclusions

A high performance computing based hydrothermal finite element simulator was developed so that a problem of city-scale geothermal utilization for community energy resilience can be investigated in the next stage of this project. The code uses an integrated parallelization scheme to compute the subsurface temperature and pressure variation during heat injection or extraction into the ground. The code leverages the deal.II finite element open-source library and the parallel programming library PETSc. The performance of the code was validated and tested by comparing the results to those of the commercial finite element software COMSOL Multiphysics. The improved computational efficiency of the new code with increasing processor number was demonstrated when compared to the efficiency of COMSOL. The advantage of using the distributed parallelization scheme against the shared parallelization scheme was also demonstrated. A city-scale Treasure Island model, which included 1013 energy piles installed in the island as part of its redevelopment project, was simulated to test whether the code can handle a large-scale simulation.

The study reported in this report mainly focuses on the implementation of parallelization scheme on the coupled hydrothermal code to realize the city-scale underground response to geothermal production. The preliminary validation of the code shows its promise, but more testing is required to improve its computational efficiency. The assumptions made for the Treasure Island case are rather simplistic. The three test cases for the **Treasure Island are just the tip of the iceberg in terms of exploring variability at the moment, but that we were able to do these three 'relatively easily' is to test the performance of the developed code**, Future extension includes seasonal loading effects, the heterogeneity of model parameters, more realistic geometry, tidal effects, etc. Such work will be carried out in the next phase of the code development.

It is also proposed to couple the current code to the system dynamics code Dymola and building physics code Modelica through FMI to carry out an integrated above-ground buildings and subsurface geothermal system simulation. Meanwhile, a geomechanics model will be added so that the subsurface water flow and ground deformation response and their effects on piles or wellbores can be assessed.

Acknowledgments

This work was supported by (i) the U.S. Department of Energy, Office of Energy Efficiency and Renewable Energy (EERE), Office of Technology Development, Geothermal Technologies Office (GTO), under Award Number DE-AC02-05CH11231 with LBNL and (ii) the National Science Foundation, Award Number #1903296 “CMMI-EPSRC: Modeling and Monitoring of Urban Underground Climate Change (MUC2)”. We thank ENGEO for providing geotechnical details relating to the Treasure Island site.

Appendix A - Treasure Island Phasing & Development

The Treasure Island redevelopment project is planned to take place in different phases to accommodate different needs and help meet the urgent demands from the project developers, as shown in **Figs A-1 to A-4**. The dates shown do not reflect the current timeline of the redevelopment project since the project has been significantly delayed over the last few years due to municipal permissions and additional concerns from the project development body. The updated progress currently includes the geotechnical field exploration and soil improvement on various places on the Treasure Island.

Phase 1 (**Fig. A-1**) is composed of the development and improvement of a causeway between Treasure Island and Yerba Buena Island, construction of a viaduct at the same location, the rehabilitation and improvement of the current shoreline perimeter and the construction of a ferry quay.

In Phase 2 (**Fig. A-2**), the progress is planned to include the improvement of Cityside and Clipper Cove Neighborhoods, construction of a historic adaptive school, Wetlands, Urban Core and Yerba Buena Island West and Open Space. The envisioned timeline for the completion of Phase 2 is planned as two years even though the most up-to-date timeline is not yet known.

The Phase 3 (**Fig. A-3**) consists mainly of the development of the Eastside Neighborhood of Treasure Island, Ballfields, the East side of Yerba Buena Island and the historic areas of the same Island. Being similar to Phase 2, the proposed timeline and the amount of time for the completion of Phase 3 is envisioned as two years.

Phase 4 is the final stage of the redevelopment (**Fig. A-4**). Cityside Neighborhoods in Treasure Island are planned to be constructed. In addition, the Core Towers and Urban Park as well as the remainder of Great Park are planned to be constructed.



Figure A-1: Treasure Island redevelopment project Phase 1 (ENGEIO Inc 2009)

Phase Two | 2012 - 2014

Cityside and Clipper Cove Neighborhoods | Historic Adaptive Re-use School | Wetlands | YBI West and Open Space | Urban Core | WWTP



Figure A-2: Treasure Island redevelopment project Phase 2 (ENGEO Inc 2009)

Phase Three | 2014 - 2016

Eastside Neighborhood | Ballfields | YBI East | YBI Historical



Figure A-3: Treasure Island redevelopment project Phase 3 (ENGEO Inc 2009)

Phase Four | 2016 - 2018

Cityside Neighborhood | Core Towers | Urban Farm | Remainder of Great Park



Figure A-4: Treasure Island redevelopment project Phase 4 (ENGE0 Inc 2009)

Appendix B – Geology at the Treasure Island redevelopment site

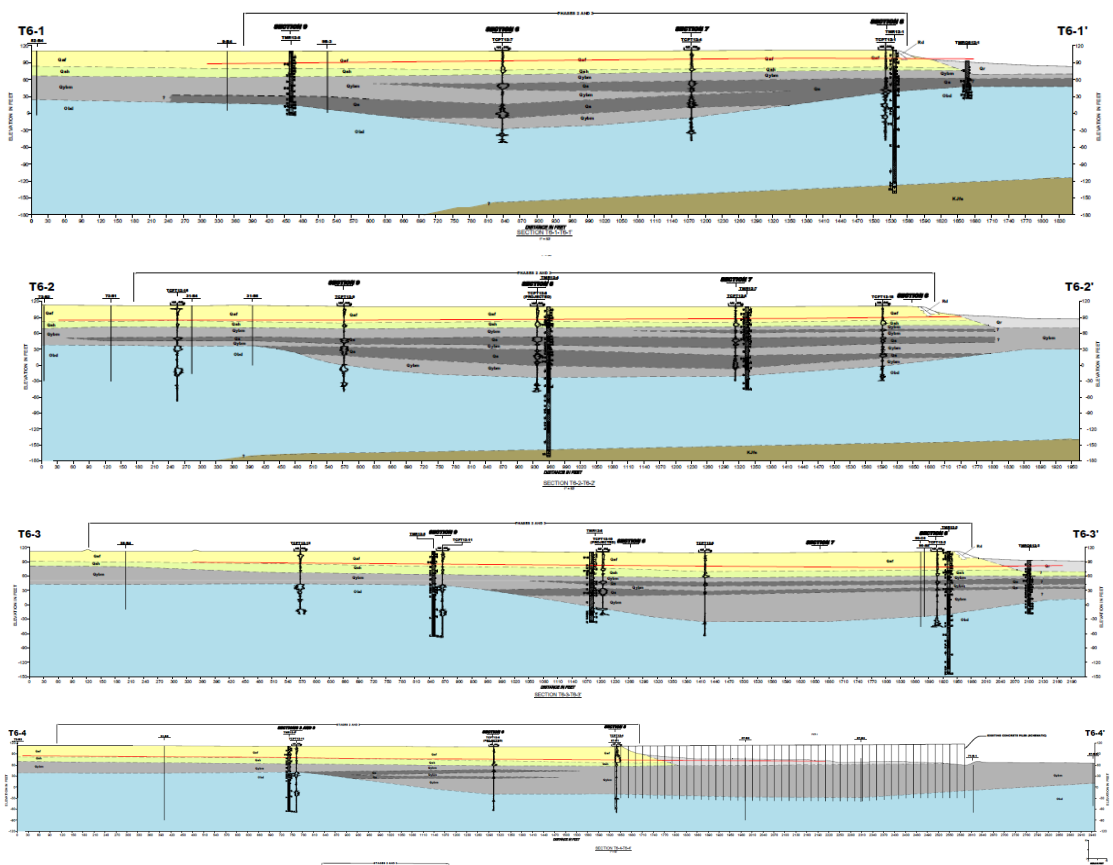
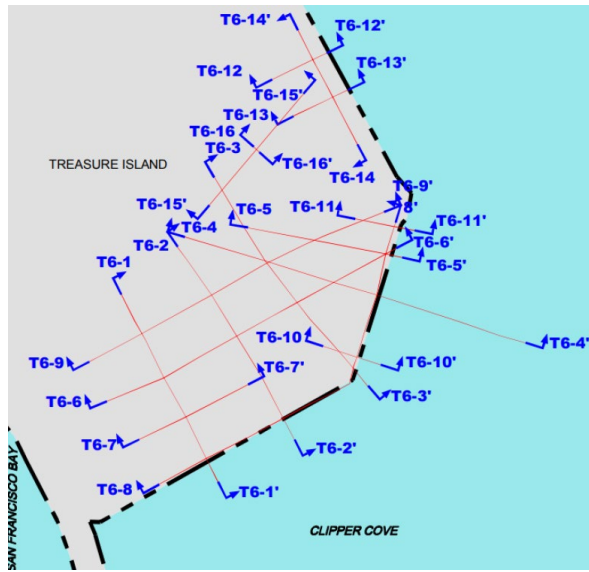
A collaborating consulting company, ENGEO, has served as the main geotechnical consultant for the ongoing real estate developments on Treasure Island (2009, 2014, 2016, 2019). The corresponding geotechnical and geological data were gathered together from their reports for the "Treasure Island Community Development" project, which is financed by a private real estate development firm.

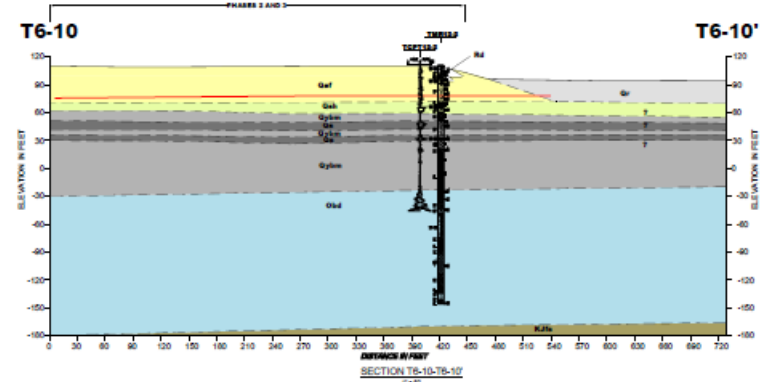
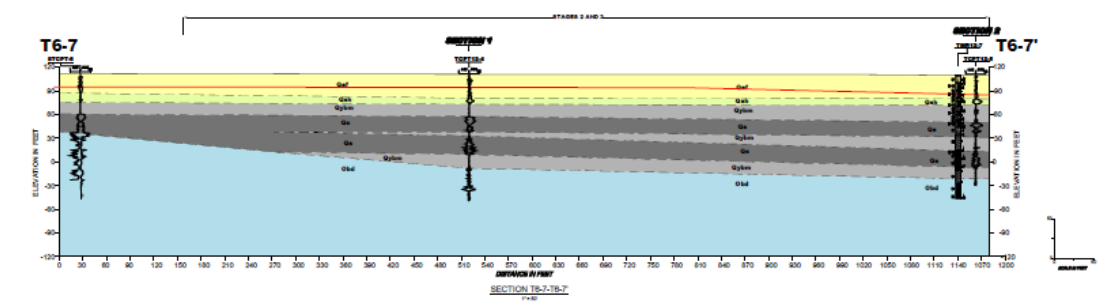
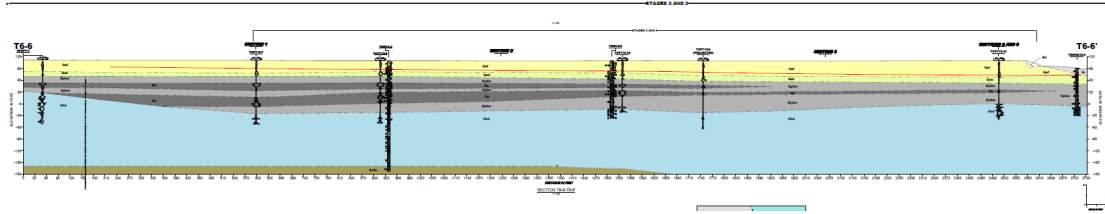
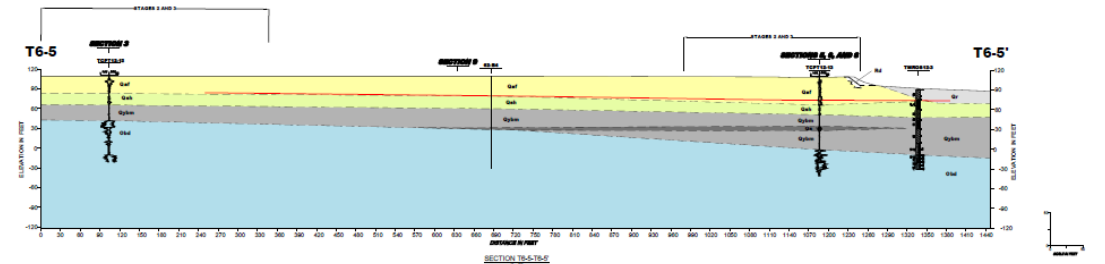
ENGEO's field exploration started with drilling three exploration borings and advancement of fifteen cone penetration test (CPT) soundings in 2014. The depths of the exploratory borings varied between 30-50 m while the depths of the CPT soundings varied between 27 and 50 m. ENGEO investigated three main sites, which are located at the southeast, southwest and northeast parts of the island. ENGEO also retrieved soil samples for conducting laboratory tests to determine the geotechnical properties of the soils at the sites. The laboratory tests included: Determination of moisture content by mass (ASTM D2216 46), determination of density (ASTM D7263 13), amount of material in soils finer than No. 200 sieve (ASTM D1140 39), particle-size analysis of soil (ASTM D422 88), liquid limit-plastic limit plasticity index (ASTM D4318 16), unconfined compression strength (ASTM D2166 5), consolidated undrained triaxial compression (ASTM D4767 6), unconsolidated undrained compression (ASTM D2850 10), laboratory miniature vane shear (ASTM D4648 37), and consolidation tests using incremental loading (ASTM D2435)

One of the most important features that is required to model the subsurface conditions is the groundwater table profile beneath the surface. For determining the elevation of the groundwater level, ENGEO conducted pore pressure dissipation tests during cone penetration tests. The reported groundwater elevation is consistent for the years 2014 and 2019, where the values vary between 101 and 106 feet (The elevation datum applied to the project is the North American Vertical Datum of 1988 (NAVD88) plus 100 feet).

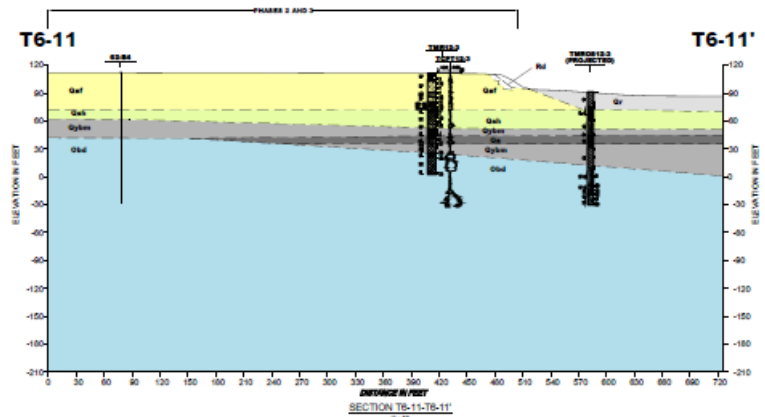
An extensive set of boring logs combined with laboratory tests enabled ENGEO to obtain the soil properties regarding water content, Atterberg limits, moisture content and soil unit weight. All of these soil properties are important in the coupled hydrothermal modeling of the Treasure Island underground for the application of community-scale geothermal energy because the soil properties differ along the profile of the island. It is possible to capture an accurate model by combining the boring logs recorded for different locations along the island and generating cross sectional profiles on that.

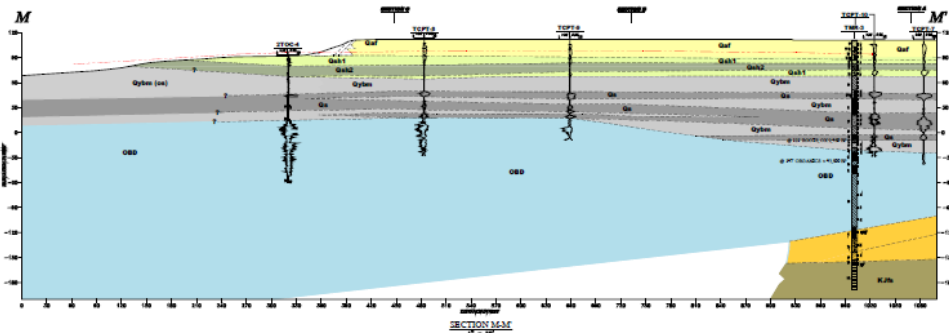
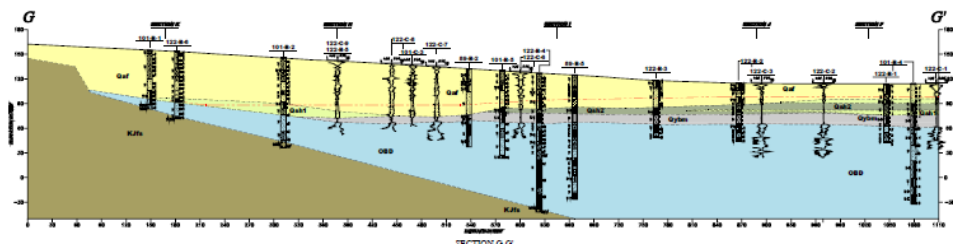
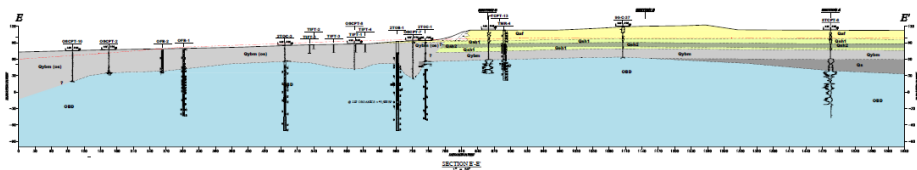
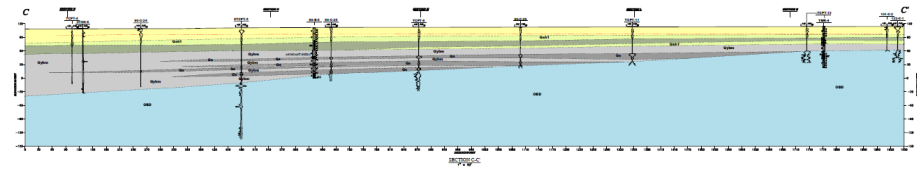
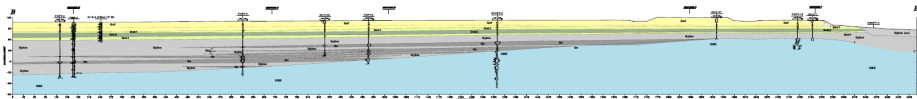
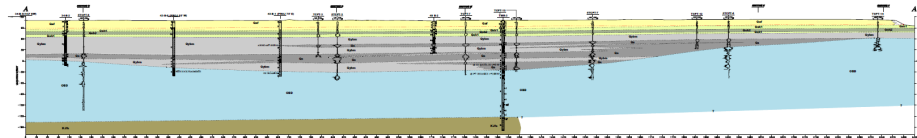
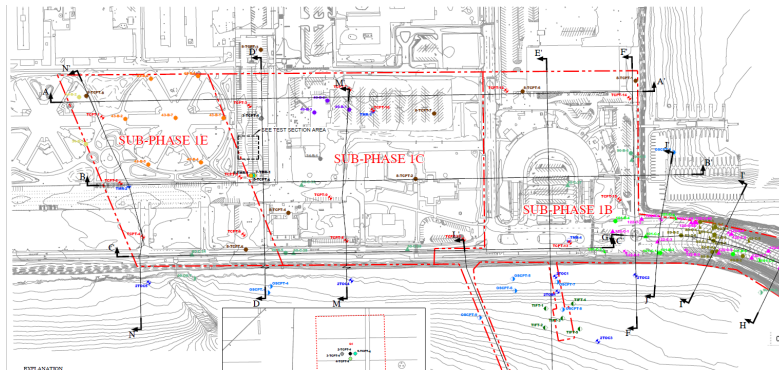
Comparing Fig. B-1, Fig. B-2, Fig. B-3 and Fig. B-4, it is shown that the fill used for the construction of Treasure Island was composed of fine to coarse loose sand and soft mud, with percentages of 65 and 35 in volume, respectively. The first 12 m of Treasure Island fill is sand, with samples above a depth of 6 m contain as much as 17 % fines. Beneath the sand fill, 3 m of native silty clayey sand followed by 27 m of soft to stiff clay with interbedded sand layers have been recorded. Sandstone and shale bedrock are reported to occur at a depth of 87 m. The water table is about 2 m below the ground surface. According to this soil profile, beneath the artificial fill, Holocene Bay sediments are observed up to 40 m. Between depths of 40 m and 90 m, Pleistocene Bay sediments are recorded. The same study concludes that the top of the Franciscan bedrock is encountered at a depth around 90 m. Fig. B-5 shows the cross section of the whole island in which layered deposits in the vertical direction are observed.





a





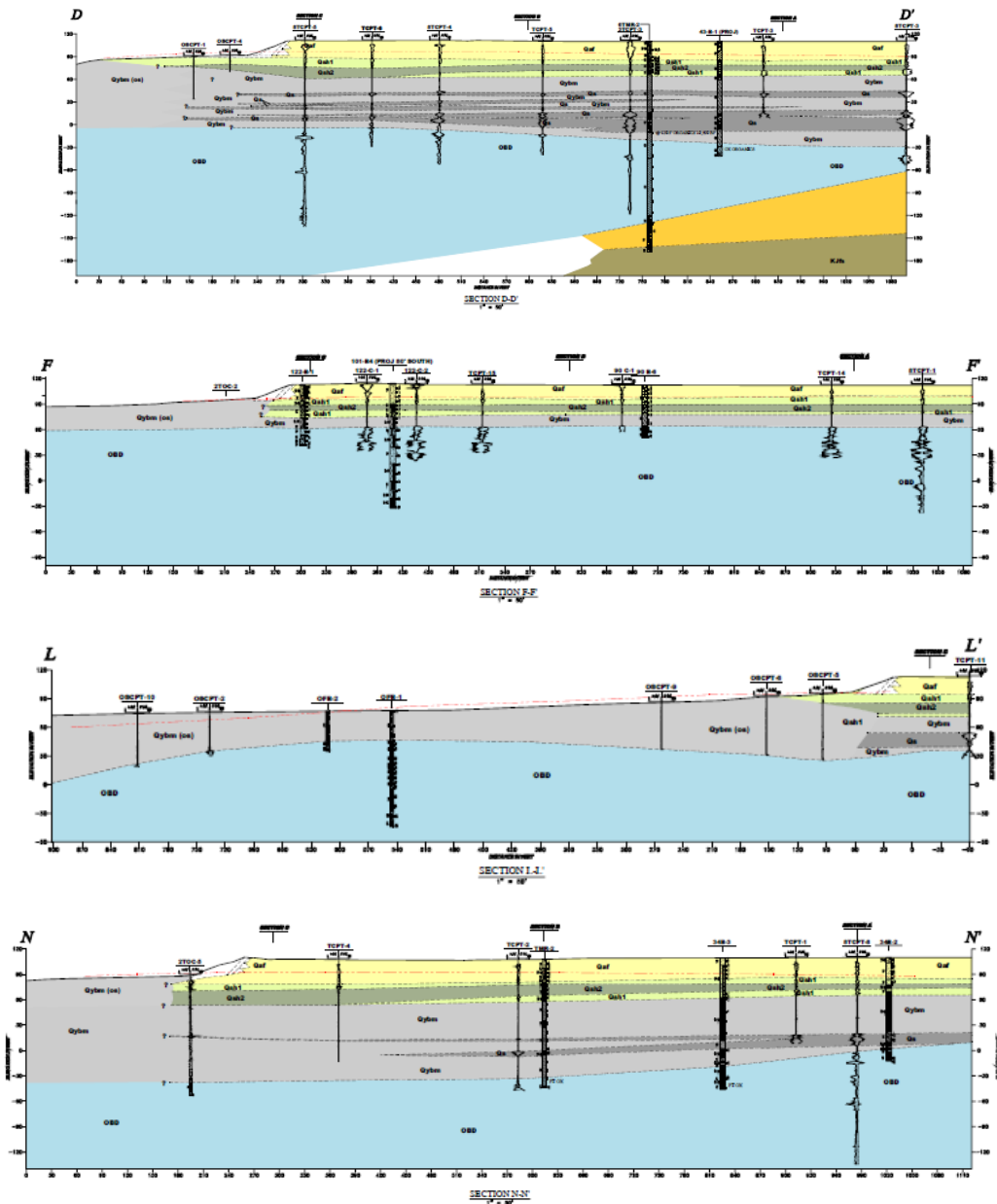


Fig. B-2 Geological cross section in the southwest part of Treasure Island (ENGENO Inc. 2014)

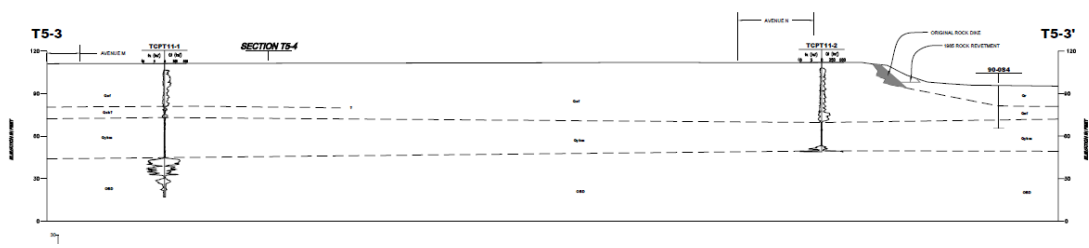
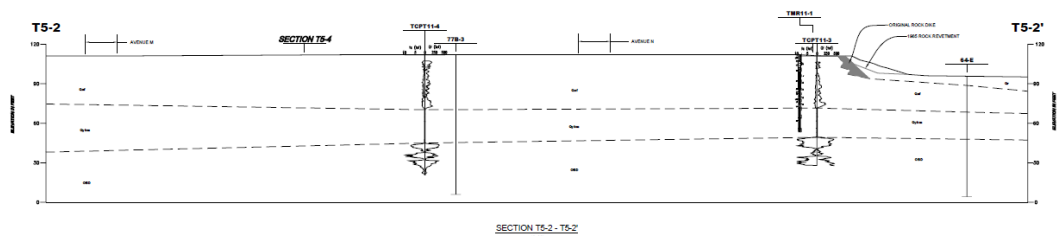
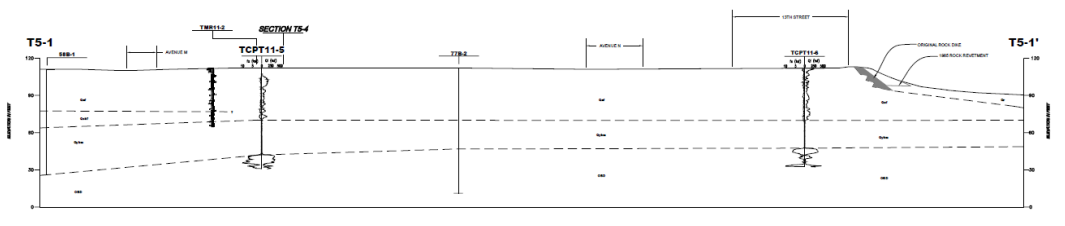
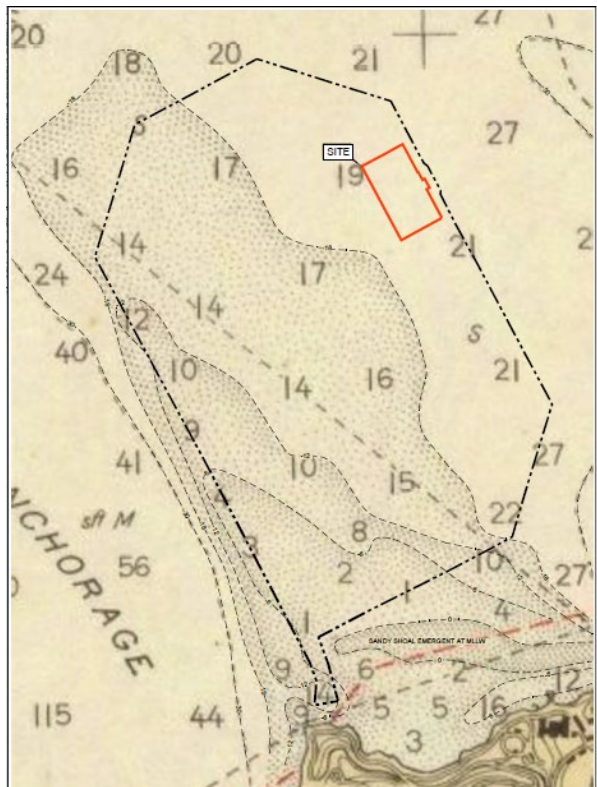


Fig. B-3 Geological cross section in the northeast part of Treasure Island (courtesy of ENGeo)

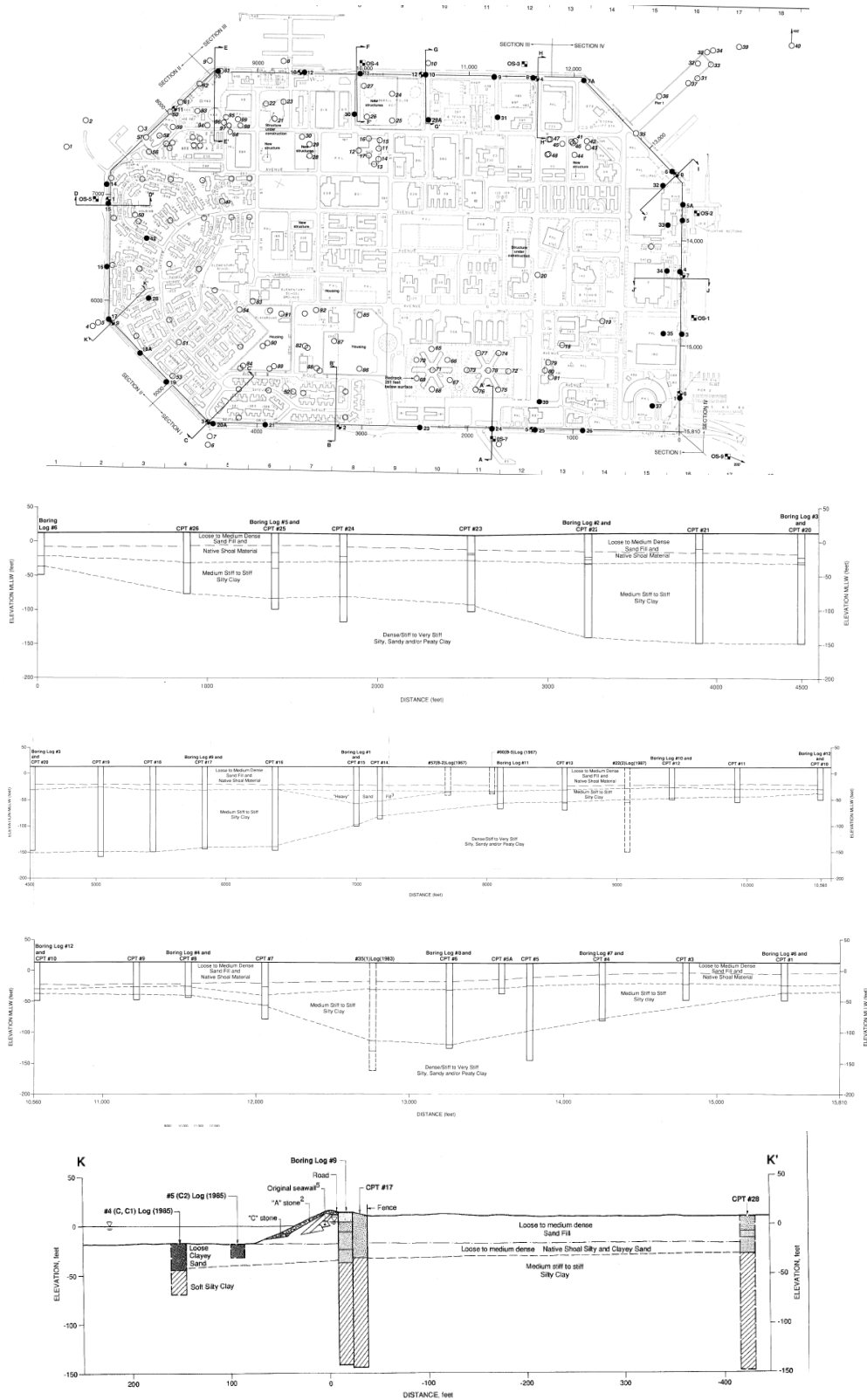
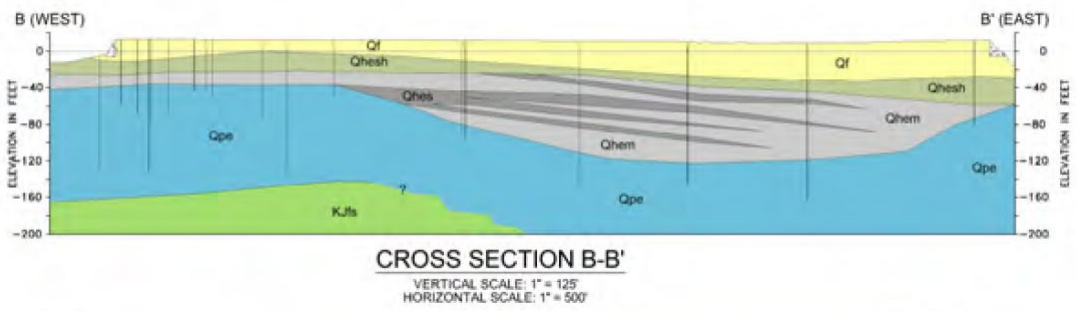
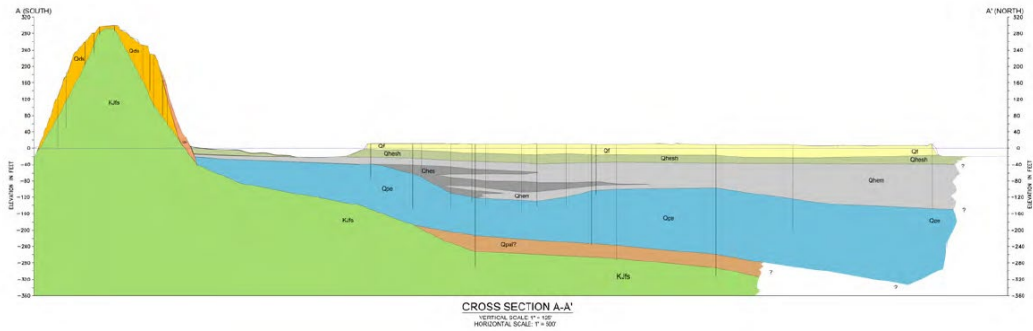
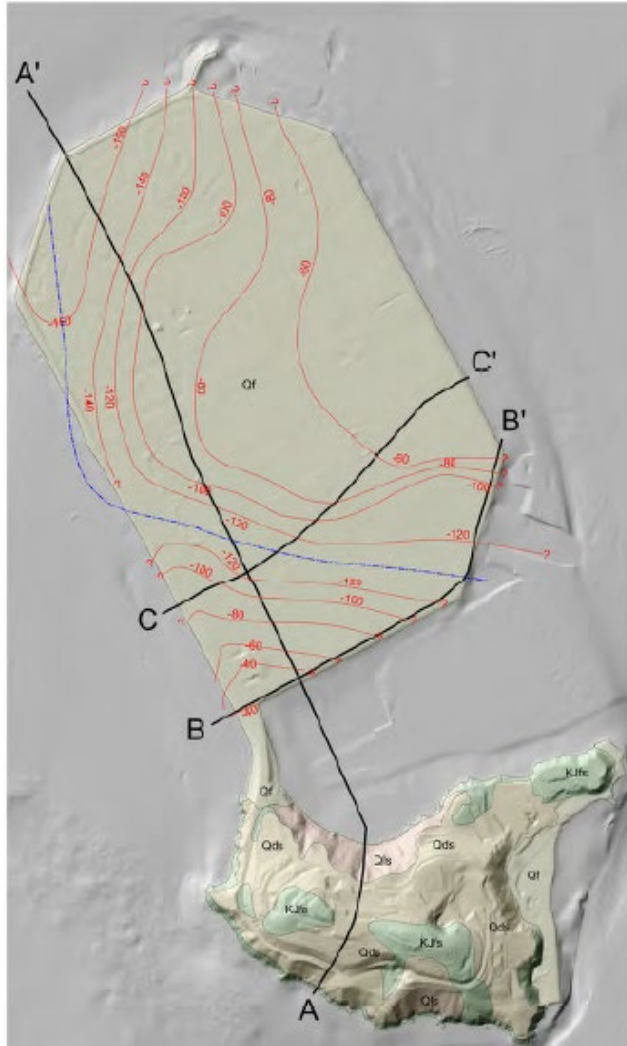
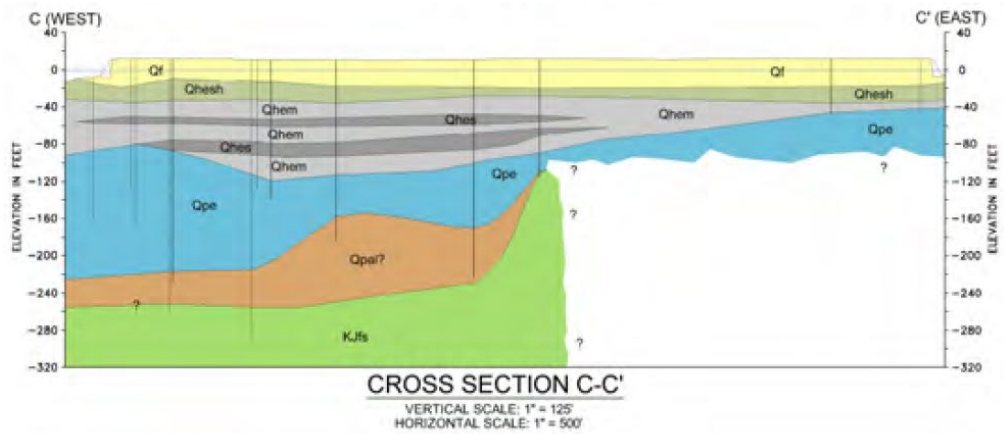


Fig. B-4 Geological cross section along the coastline of Treasure Island (ENGE0 Inc. 2009)





EXPLANATION

- - - - - PROBABLE PALEO-CHANNEL
- ~ -20 ELEVATION CONTOURS ON TOP OF OLDER BAY DEPOSITS*
- Qf HYDRAULIC FILL
- Qls LANDSLIDE
- Qos EOLIAN SAND
- Qhesh SHOAL SAND
- Qhem HOLOCENE ESTUARINE CLAYS (BAY MUD)
- Qhes HOLOCENE ESTUARINE SANDS
- Qpe LATE PLEISTOCENE ESTUARINE DEPOSITS (OLD BAY DEPOSITS)
- Qpal? LATE PLEISTOCENE ALLUVIUM
- KJfs FRANCISCAN ASSEMBLAGE BEDROCK
- | LOCATIONS OF BORINGS DEPICTED ON CROSS SECTIONS

Fig. B-5 Geological cross section of Treasure Island (Johnson and Bartow, 2018)

References

- Adam, D., and Markiewicz, R., 2009. Energy from earth-coupled structures, foundations, tunnels and sewers. *Géotechnique*, 59(3), pp. 229-236.
- Alzetta, G., Arndt, D., Bangerth, W., Boddu, V., Brands, B., Davydov, D., Gassmöller, R., Heister, T., Heltai, L., Kormann, K., and Kronbichler, M., 2018. The deal. II library, version 9.0. *Journal of Numerical Mathematics*, 26(4), pp.173-183.
- Amis, T., Robinson, C., Wong, S., 2010. Integrating geothermal loops into the diaphragm walls of the Knightsbridge Palace Hotel project. *EMAP-Basements and Underground Structures 2010*.
- Andrus, R.D., Chung, R.M., Stokoe II, K.H., and Bay, J.A., 1998. Delineation of densified sand at Treasure Island by SASW testing. In: *Geotechnical site characterization*, P.K. Robertson and P.W. Mayne, eds., Proceedings of the First International Conference on Site Characterization, ISC'98, Atlanta, Georgia, USA, A.A. Balkema, pp. 459-464.
- Arndt, D., Bangerth, W., Davydov, D., Heister, T., Heltai, L., Kronbichler, M., Maier, M., Pelteret, J.P., Turcksin, B., and Wells, D., 2020. The deal. II finite element library: Design, features, and insights. *Computers & Mathematics with Applications*.
- Ashford S.A., and Rollins, K.M. 2002. The Treasure Island liquefaction test: final report, University of California, San Diego, Structural Systems Research Project, Report No. SSRP-2001/17.
- Baise, L.G., Glaser, S.D., and Dreger, D., 2003. Site response at Treasure and Yerba Buena Islands, California. *Journal of Geotechnical and Geoenvironmental Engineering*, 129(5), pp. 415-426.
- Balay, S., Abhyankar, S., Adams, M., Brown, J., Brune, P., Buschelman, K., Dalcin, L., Dener, A., Eijkhout, V., Gropp, W. and Karpeyev, D., 2019. *PETSc users manual*.
- Bourne-Webb, P.J., Amatya, B., Soga, K., Amis, T., Davidson, C. and Payne, P., 2009. Energy pile test at Lambeth College, London: geotechnical and thermodynamic aspects of pile response to heat cycles, *Géotechnique*, 59(3), 237-248.
- Brandl, H., 2006. Energy Foundations and other thermo-active ground structures. *Geotechnique*, No.2: 81-122.
- [City and County of San Francisco Urban Ground Source Heat Pumps – Phase I](#)
- ENGEO Inc. Geotechnical Conceptual Design Report for Treasure Island. 2009.
- ENGEO Inc. Geotechnical Data Report for Treasure Island Sub-Phase 1A. 2014.
- ENGEO Inc. Dynamic Behavior of the Treasure Island Natural Shoal Deposit. 2016.
- ENGEO Inc. Geotechnical Characterization Report for Treasure Island Stages 2 and 3. 2019.
- Frohne, J., Heister, T., and Bangerth, W., 2016. Efficient numerical methods for the large-scale, parallel solution of elastoplastic contact problems. *International Journal for Numerical Methods in Engineering*, 105(6), pp. 416-439.
- Goto, S., Yamano, M., Morita, S., Kanamatsu, T., Hachikubo, A., Kataoka, S., ... & Matsumoto, R., 2017. Physical and thermal properties of mud-dominant sediment from the Joetsu Basin in the eastern margin of the Japan Sea. *Marine Geophysical Research*, 38(4), pp.393-407.
- Johnson, K.A., and Bartow, G.W., eds., 2018. *Geology of San Francisco, California, United States of America*, *Geology of Cities of the World Series*, Association of Engineering Geologists, 183 p.
- Koňáková, D., Vejmelková, E., & Černý, R., 2013. Thermal properties of selected sandstones. In *Advances in modern mechanical engineering: Proceedings of the 4th International Conference on Fluid Mechanics and Heat & Mass Transfer (FLUIDSHEAT'13)*, Dubrovnik, Croatia, 25–27 June 2013, pp. 100-104.
- Lee, C.H., and Praszker, M., 1969. Bay mud developments and related structural foundations. *Geologic and engineering aspects of San Francisco Bay fill*, H.B. Goldman, ed., California Division of Mines and Geology Special Report, 97, pp. 41-86.

- Misra, A., Becker, B.R., & Fricke, B.A., 1995. A theoretical model of the thermal conductivity of idealized soil. HVAC&R Research, 1(1), 81-96.
- Nicholson, D. P., Chen, Q., Pillai, A., and Chendorain, M., 2013. Developments in thermal pile and thermal tunnel linings for city scale GSHP systems, In: Proceedings, 38th Workshop on Geothermal Reservoir Engineering, Stanford University, 8 p.
- Nguyen, H.Q., 2006. Reanalysis of the settlement of a levee on soft bay mud. Doctoral dissertation, Massachusetts Institute of Technology.
- Phillips, S.P., Hamlin, S.N., & Yates, E.B., 1993. Geohydrology, water quality, and estimation of ground-water recharge in San Francisco, California, 1987-92. US Geological Survey Water-Resources Investigations Report 93-4019, 69 p.
- Power, M.S., Egan, J.A., Shewbridge, S.E., deBecker, J., and Faris, J.R., 1998. Analysis of liquefaction-induced damage on Treasure Island. In: The Loma Prieta, California, Earthquake of October 17, 1989 —Liquefaction, T.L. Holzer, ed., U.S. Geological Survey Professional Paper 1551-B, pp. 87-120.
- Russo, S.L., & Civita, M.V. ,2009. Open-loop groundwater heat pumps development for large buildings: a case study. Geothermics, 38(3), 335-345.
- Saad, Y. and Schultz, M.H., 1986. GMRES: A generalized minimal residual algorithm for solving nonsymmetric linear systems. SIAM Journal on scientific and statistical computing, 7(3), pp.856-869.
- Soga, K. and Y. Rui, "Energy Geostructures," edited by S.J. Rees, Advances in Ground-Source Heat Pump Systems, Woodhead Publishing Ltd., 2016, pp. 185-221
- Suckling, T.P., and Smith, P., 2002, Environmentally friendly geothermal piles at Keble College, Oxford, UK, Deep Foundations Institute Conference, Nice, France.
- Walters, M.A., and Combs, J., 1991. Heat flow in The Geysers-Clear Lake geothermal area of northern California, U.S.A. In: Monograph on The Geysers Geothermal Field, Geothermal Resources Council Special Report No. 17, 43-53.
- Williamson, K. H., 1991. Development of a reservoir model for The Geysers geothermal field. on The Geysers Geothermal Field, Geothermal Resources Council Special Report No. 17, 179-187.